

# **Quantifying Surface Water and Groundwater Exchanges in the Southern Albuquerque Basin**

by

Ethan Williams

Submitted in Partial Fulfillment  
of the Requirements for the Degree of  
Master of Science in Hydrology



New Mexico Institute of Mining and Technology  
Socorro, New Mexico  
March, 2023

## ABSTRACT

Aridification and overallocation of water has exacerbated water stress in the American Southwest. Along the Rio Grande groundwater discharge augments surface flows but also contributes a disproportionate amount of solute to the river. We used environmental tracers and differential flow gauging to characterize the volume and provenance of groundwater inflow, which is geochemically diverse and derived from multiple sources (e.g. upwelling brine, shallow alluvial groundwater, recharge from local bedrock watersheds, irrigation return flows) along a 70-km interval overlying the southern extent of the Albuquerque Basin of the Rio Grande Rift, wherein structural controls force various flow paths to converge. Previous studies focus on the role of deeply sourced brines on river salinization without considering shallower sources. Synoptic sampling of the Rio Grande and adjacent irrigation drains was performed five times throughout 2021. Water samples were analyzed for major and minor anions and cations, trace metals,  $^{87}\text{Sr}/^{86}\text{Sr}$ ,  $^{222}\text{Rn}$ ,  $\delta^{18}\text{O}$ , and  $\delta^2\text{H}$ . Mixing analysis using  $^{87}\text{Sr}/^{86}\text{Sr}$  vs.  $1/[\text{Sr}]$  indicated a three-endmember system including upwelling sedimentary brine, shallow saline groundwater influenced by Paleozoic strata, and through-flowing water of the Rio Grande. Upwelling sedimentary brine was concentrated in the distal basin and near an intra-basin bedrock high, and accounted for as much as 4% of flow in irrigation drains and 1% of flow in the Rio Grande. Paleozoic-influenced water was associated with southern basin tributary systems and accounted for as much as 21% of flow in irrigation drains and 13% of flow in the Rio Grande. Mixing processes and mineral interactions result in a seasonally variable transition from  $\text{Ca}^{2+}\text{-HCO}_3^-$  water type in the north to a  $\text{Na}^+\text{-HCO}_3^-$  water type in the south of the project area. Groundwater flux rates ranged from -13.1 to 23.0  $\text{m}^3/\text{d}/\text{m}$  in irrigation drains. Seasonal trends in river discharge and irrigation mediate the volume and relative influence of saline groundwater inflows, which had the greatest influence during pre-irrigation baseflow conditions in March where chloride concentrations in the river increased from 21.2 to 50.5  $\text{mg}/\text{L}$  across the extent of the project area. Our findings reinforce the understanding that geologic sources are the primary driver of Rio Grande salinization and demonstrate that shallow tributary associated flow paths are volumetrically and chemically significant components of flow.

## ACKNOWLEDGMENTS

This project was made possible by the Middle Rio Grande Conservation District (MRGCD), who presented the grant opportunity and funded a proposal submitted by Alex Rinehart and Dan Cadol. MRGCD funding covered two years of graduate salary and provided additional project funds. Guidance and help from MRGCD personnel was a major asset to the design and execution of this study. Anne Marken (MRGCD water ops division manager) provided enormous support to our efforts, as well as Jessica Howe and Jeremy DeArmond (MRGCD hydrologists). Additional funding was provided by the New Mexico Water Resource Research Institute (NM WRRI), the New Mexico Geological Society (NMGS), and the New Mexico Tech Earth & Environmental Science (E&ES) department. These sources provided the funding necessary to complete the majority of the numerous water analyses performed in this study.

Bonnie Frey and Dustin Baca of the New Mexico Bureau of Geology and Mineral Resources Analytical Chemistry Lab provided an incredible amount of help in regard to the analysis of the project's water samples. The lab allowed me to help perform the analyses in return for a discounted rate, and this opportunity allowed this study to include the number of sites and campaigns that are presented herein. The help that Bonnie and Dustin provided was instrumental to this study, and their instruction gave me a bounty of insight and skills in the field of analytical chemistry.

Lin Ma of the University of Texas at El Paso (UTEP) Earth, Environmental, and Resources Department was an essential contributor to this study. He not only agreed to serve on the author's committee and guided our interpretation of the strontium isotopes and mixing system but administered the  $^{87}\text{Sr}/^{86}\text{Sr}$  analyses himself. These analyses provided the backbone of this study's results and we are grateful for his generous support.

Alex Rinehart and Dan Cadol co-wrote the grant that started this project and served as project co-P.I.s and thesis committee members. Throughout the course of the project Alex and Dan provided close support in all aspects of the study, from fieldwork to interpretation. They excelled as mentors, educators, and collaborators. Dan effectively oversaw the study's surface water component and made himself available to lend support whenever possible. Alex served as the author's research advisor. Not only did he take great personal responsibility for the success of the study – he put himself forward as a mentor. Alex led by example, demonstrating quality research practices and a rigorous work ethic. He invested substantial time and resources into this project and trusted me to take a lead role in the project's design and implementation. I am incredibly grateful to the attention that he gave to my success and the success of this project, he and Dan both have my utmost respect as individuals, teachers, and scientists.

## TABLE OF CONTENTS

ABSTRACT.....	i
ACKNOWLEDGMENTS .....	ii
Table of Contents.....	iii
I. LIST OF TABLES .....	v
II. LIST OF FIGURES .....	vi
Preface	ix
 CHAPTER 1 - Introduction.....	 1
1.1 Overview.....	1
1.2 Background.....	5
1.2.1 Project Area Overview.....	5
1.2.2 Regional Geology .....	6
1.2.3 Hydrology .....	8
1.2.4 2021 Rio Grande Flow History .....	10
 CHAPTER 2 - Methods.....	 12
2.1 Site descriptions and overview .....	12
2.1.1 RM 165: Bosque Farms .....	12
2.1.2 RM 155: Tome.....	13
2.1.3 RM 141: Bosque .....	13
2.1.4 RM 135: Abeytas .....	13
2.1.5 RM 124: La Joya.....	14
2.1.6 RM 116: San Acacia .....	14
2.2 Flow Gauging.....	14
2.2.1 Differential Flow Gauging .....	14
2.2.2 Estimating Inflow Rate from Radon Activity .....	15
2.3 Water Sampling and Analysis.....	16
2.4 Geochemical Analysis .....	16

2.4.1	Saturation Indices.....	17
2.4.2	Evaporation .....	17
2.4.3	Strontium isotope analysis .....	17
CHAPTER 3 - Results .....		19
3.1	Rates of Groundwater Flux .....	19
3.1.1	Overview .....	19
3.1.2	Radon Inflow .....	20
3.1.3	Physical Flow Gauging .....	21
3.2	Water Chemistry .....	24
3.2.1	Field Parameters.....	25
3.2.2	Major Ions .....	26
3.2.3	Trace Metals.....	29
3.2.4	Stable Isotopes .....	31
3.2.5	Strontium Isotopes .....	32
3.2.6	Mineral Saturation Indices .....	34
CHAPTER 4 - Discussion .....		36
4.1	Discharge Trends .....	36
4.2	Trends in Geochemistry and Water Isotopes .....	39
4.3	Mixing Analysis.....	42
CHAPTER 5 - Conclusion.....		50
5.1	Overview.....	50
5.2	Management recommendations .....	53
Concluding Remarks.....		54
References.....		55

## LIST OF TABLES

Table	Page
Table 3.1. Length of upstream drain network above drain site sample locations.....	20
Table 3.2. Dilution gauging results.....	22
Table 3.3. Conventional Gauging results.....	23
Table 3.4. Drain water evaporation calculated following Clark (2015).....	32
Table 3.5. River water evaporation for May and October calculated following Clark (2015).....	32
Table 4.1. Radon activity and inflow rate overview.....	38
Table 4.2. Table of end-member fractions by [Sr] vs. $^{87}\text{Sr}/^{86}\text{Sr}$ mass balance calculations.....	49

## LIST OF FIGURES

Figure	Page
Figure 1.1. Overview of the project area and the regional geologic setting. (a) shows the location of the Albuquerque basin and the geology of the simplified area. (b) shows the location of the project area and the Rio Grande Rift in reference to the state of New Mexico.....	4
Figure 1.2. Rift fill thickness within the Southern Albuquerque Basin showing site locations, the Rio Grande and major tributaries, and physiographic and structural features.....	7
Figure 1.3. Soil Surface Salt Concentration and SAR in the MRGCD Belen District.....	8
Figure 1.4. Hydrogeochemical groundwater zones and predevelopment groundwater contours of the Southern Albuquerque basin.....	9
Figure 1.5: (a) 2021 surface water diversions/returns made by the Albuquerque Bernalillo County Water Authority (ABCWA). (b) 2021 Rio Grande discharge records from USGS gages in the project area. (c) Schematic map showing sample locations, USGS gages, and ABCWA river diversion and return locations.....	11
Figure 3.1. Symbol key schematic showing site locations and their river mile designation. The color and shape of the symbols correspond with the subsequent figures.....	20
Figure 3.2. Specific conductivity trends along flow distance by campaign for rivers and drains.....	25
Figure 3.3. Boxplot of major ion proportions and major water types of samples during each campaign.....	27
Figure 3.4. Cl <sup>-</sup> concentration (ppm) along flow distance in drains and the Rio Grande during individual measurement campaigns.....	28
Figure 3.5. Trends in Cl <sup>-</sup> mass flux (kg/day) along flow distance in drains and the Rio Grande during individual measurement campaigns.....	29
Figure 3.6. Spiderplots of trace metal concentration (ppm) of all samples by month.....	30
Figure 3.7. Monthly trends in $\delta^{18}\text{O}$ vs. $\delta^2\text{H}$ of drain and river samples colored by river mile. Data from Mills (2001) collected in the project area during January and August of 2001 is shown on plots (f) and (e) respectively.....	31
Figure 3.8. Strontium isotope trends along flow distance by campaign for the river and drains.....	33
Figure 3.9. Saturation indices (SI) of select minerals calculated from surface waters.....	35

Figure 4.1. Samples and endmembers in $1/[Sr]$ vs. $^{87}Sr/^{86}Sr$ mixing space.....	45
Figure 4.2. Spatial distribution of mixing fractions as determined by the upstream river composition as the Rio Grande end member. Composition and location are given by pie chart. ....	46
Figure 5.1. 3-D basin fill thickness and surface topography of the southern Albuquerque basin showing the site locations and interpreted flow path distribution of end-member waters identified in this study.....	51



The dissertation is accepted on behalf of the faculty Institute by the following committee:

Alex Rinehart

---

Academic and Research Advisor

Daniel Cadol

---

Committee Member

Lin Ma

---

Committee Member

I release this document to the New Mexico Institute of Mining and Technology.

Ethan Williams

December 31, 2022

---

## PREFACE

This study was performed to satisfy the requirements for a M.S. in Hydrology at New Mexico Tech under the advisement of Alex Rinehart with the goal of characterizing end-member water contributions and groundwater flux rates within the Middle Rio Grande Conservation District (MRGCD). The study was sponsored by and performed in collaboration with the MRGCD. Daniel Cadol and Alex Rinehart served as the project's Principal Investigators. Additional funding was provided by the New Mexico Water Resource Research Institute, the New Mexico Geological Society, and the New Mexico Tech Earth and Environmental Sciences department through the Rob Bowman Endowment.

The study was designed to provide a characterization of how groundwater affects irrigation drains and the Rio Grande in the Southern Albuquerque Basin, which has implications for water management and the overall hydrogeologic characterization the basin – which is an ongoing topic of scientific inquiry. Our approach involved synoptic sampling of volumetric flows and water chemistry analysis in the irrigation drains, with additional water chemistry samples collected from the river. This sampling method allowed us to quantify baseflow volumes and water provenance (the irrigation drain measurements) and evaluate how baseflow impacts the river. The spatial scale of our analysis covered the entirety of the Belen District of the MRGCD – which is a distinct management boundary that is coincident with the southern Albuquerque Basin. The timeline of our sampling campaigns included pre-irrigation season, irrigation season itself, and post-irrigation season. The approach, extent, and timeline of this study provides a uniquely thorough characterization of flow dynamics in the basin that is practically and scientifically relevant.

We employed a variety of methods to characterize both flow dynamics and geochemical processes. Groundwater flux in the drains were determined using differential flow gauging by two methods (conventional flow gauging and dilution gauging with rhodamine dye), as well as calculated based of the activity of radon in water. Trends in river discharge were evaluated from USGS gauge data. End member characterization, mixing patterns, and geochemical trends were characterized using a broad set of environmental tracers including major and minor anions and cations, trace metals,  $^{87}\text{Sr}/^{86}\text{Sr}$ ,  $\delta^{18}\text{O}$ ,  $\delta^2\text{H}$ , and field parameters.

The results of this study include the development of a conceptual model of the surface water/groundwater mixing system. We believe groundwater discharge into the drains is sourced from three endmembers: (1) through-flowing Rio Grande water (associated with the Rio Grande headwaters or northern tributaries), (2) water from local tributaries watersheds (e.g. Abo Arroyo, Rio Puerco) that interacted with evaporite and carbonate rocks and sediments in their watersheds, and (3) upwelling sedimentary brine that interacted with basement and granitic-sourced sediment. The first end member makes up the majority of discharge and has high water quality, but it is sensitive to climate and anthropogenic perturbations. The second endmember is volumetrically significant but of poor water quality and is diffusely present in the southern portion of the basin. Its poor

water quality poses a threat to river resilience. The third end member is a minor volumetric contributor but disproportionately degrades water quality. It is present exclusively in the distal basin and near at least one intra-basin bedrock high. The proportion of these endmembers varies through time in relation to seasonality, river stage, and irrigation practice.

This study is presented herein in paper format, consisting of an introduction, background, methods, results, discussion, conclusion, and concluding remarks sections. The entire dataset collected for this study including flow measurements and water sample analyses can be found in the electronic supplement. All figures were produced in RStudio 2022.07.0, ArcScene 10.7.1, and ArcMap 10.7.1 and modified in Inkscape 1.2.1. Data analysis was performed in RStudio 2022.07.0, MATLAB R2022a and Microsoft Excel version 2210. We intend to pursue publication of this work in a relevant scientific journal such as Water Resources Research, Journal of Hydrology, Chemical Geology, or similar.

# CHAPTER 1

## INTRODUCTION

### 1.1 Overview

Water resources in the Rio Grande rift are a topic of practical, political, and scientific interest. Water is a limiting resource in the rift as much as it is throughout the North American Southwest – yet outstanding questions about water resilience and sources of baseflow remain unanswered. This study seeks to resolve a present contrast between literature that emphasizes the impact on water quality of deep upwelling flows along the axis of extensional basins ((Hogan et al., 2007; Phillips et al., 2003), while more application focused work has shown that most groundwater/surface water interactions are driven by shallow groundwater flow ((Bexfield et al., 2011; S.S Papadopoulos & Associates, 2000). This work attempts to examine what is likely a continuum between these end member conceptual models within the Rio Grande in the Albuquerque basin of the Rio Grande Rift. To that end, we focus on constraining the influence of end member groundwaters on the greater system to improve our understanding of how basin-scale and local-scale hydrologic processes interact. We consider inputs from large tributaries in addition to deep axial groundwater flow and shallow river exchanges. Our efforts improve what we know about the hydrogeologic framework – or ‘plumbing’ – of the basin and informs the resilience of the system to climate change and human demands. While our application is focused on the southern Albuquerque basin, this study demonstrates how flow paths and mixing zones may be distributed in other axially drained extensional basin systems.

Aridification and overallocation of water has exacerbated water stress along the Rio Grande in terms of water quality and quantity alike ((Garcia et al., 2021; Hogan et al., 2007; Phillips et al., 2003; S.S Papadopoulos & Associates, 2000). As climate models forecast reduced snowpack and higher temperatures in the coming century (Gangopadhyay et al., 2021), the need to account for the sources of both water and solute to the Rio Grande becomes more and more essential to forecast how the river will respond to increased drought. Currently, most of the Rio Grande’s flow is derived from snowmelt in the river’s headwaters in the San Juan mountains of southeast Colorado, and is augmented by tributary inputs, local precipitation, and regional groundwater discharge. Unlike other sources of water to the Rio Grande, groundwater is buffered from the effects of climate change and can be effectively managed. As regional precipitation diminishes, groundwater can be expected to have a greater impact on the Rio Grande’s flow characteristics. However, constraining groundwater’s influence on the river is difficult due to the hydrogeologic and chemical complexity of the aquifer system.

This study focuses on a 70-km portion of the Rio Grande south of Albuquerque, NM (Figure 1.1), where structural controls at the distal end of the Albuquerque Basin of the Rio Grande Rift force groundwater flow paths associated with hydrogeochemically distinct sources to converge and mix with the riparian aquifer and surface waters. This has been documented by multiple researchers, but the processes and sources that dominate the mixing system are poorly constrained. Plummer and others (2004) documented a zone of mixed groundwater at the distal end of the basin that is a likely a combination of water from shallow groundwaters upgradient as well as older chloride-rich waters from deeper in the aquifer system, however little discussion is given to the specifics of the mixing system. Phillips et al. (2003) and Hogan et al., (2007) found stepwise increases in Rio Grande's solute load coincident with the termini of individual rift basins which they attribute to the upwelling of deep, solute-laden, basin-scale axial flow paths. In the Albuquerque basin this abrupt increase in salinity has also been attributed to mantle-derived endogenic fluids ascending along basin bounding faults (Williams et al., 2013). These works provide robust evidence that geologically derived solute is the primary source of salinity in the Rio Grande, but little consideration is given to the potential influence of saline shallow groundwaters associated with extrabasinal tributary systems (the Abo Arroyo and Rio Puerco).

The majority of groundwater characterization in the basin focuses on physical hydrogeology as opposed to water quality. Regional groundwater storage, recharge processes, and stream depletion have received particular focus, principally in the form of MODFLOW models (Bexfield et al., 2011). Regional water budgets such as the Middle Rio Grande Water Supply Study focus on inputs and outputs to the Rio Grande, including surface/groundwater exchanges (S.S Papadopoulos & Associates, 2000). Few studies rigorously explore the quantity and quality of the hydrologic system conjunctively, which presents a gap in our current understanding.

We attempt to provide an improved characterization of surface/groundwater exchange processes by (1) identifying the significant endmembers present in the surface-groundwater mixing system in the southern Albuquerque basin, (2) determining the proportion and volumetric inflow rate of endmember waters, and (3) documenting how these trends change in response to seasonal factors. To accomplish this, we performed environmental tracer analysis and differential flow gauging along a 70-kilometer reach of the Rio Grande overlying the Southern Albuquerque Basin throughout 2021. Together, these data constrain how hydrogeochemically distinct groundwater inputs affect the quality and quantity of surface flow before, during, and after irrigation season. Data analysis and interpretation focused on quantifying vectors of water and solute to the system in order to improve the overall hydrologic characterization of the system and support management decisions.

Environmental tracer analysis is frequently used in hydrologic studies to identify water provenance and geochemical processes. Tracer analysis is often focused on individual catchments or locations for the purpose of hydrograph separation (Christopherson and Hooper, 1992; Hogan et al., 2000; Stewart et al., 2022). However, larger scale multi-tracer longitudinal studies are becoming popular globally as a means to quantify watershed scale processes and resource availability (Cook, 2013; Xu et al., 2017; Zhi et al., 2019). Studies such as these employ synoptic sampling of stream discharge and chemical constituents such as major and minor ions, stable isotopes ( $^{87}\text{Sr}/^{86}\text{Sr}$ ,  $\delta^{18}\text{O}$ ,  $\delta^{11}\text{B}$

and  $\delta^2\text{H}$ ) radiogenic isotopes ( $^{222}\text{Rn}$ ,  $\delta^{234}\text{U}$ ,  $^{14}\text{C}$ ,  $^3\text{H}$ ,  $^{36}\text{Cl}$ ), and other parameters (TDS, EC, temperature) in order to identify and constrain mixing processes, inflow rates, chemical evolution, and water provenance.

Several environmental tracer studies have been conducted along the Rio Grande. Phillips et al. (2003) used  $\delta^{18}\text{O}$ ,  $\delta^2\text{H}$ ,  $\text{Cl}^-$ , and  $\text{Cl}/\text{Br}$  collected along a ~1200-km reach of the Rio Grande to demonstrate that evaporation alone cannot account for the increase of ~40 ppm TDS to >2,000 ppm TDS across that interval, and that inputs of saline groundwater coincident with bedrock highs at the termini of sedimentary basins are the dominant salinization mechanism. Hogan et al. (2007) further demonstrated the influence of saline groundwater using  $\text{Cl}/\text{Br}$ ,  $\text{Ca}/\text{Sr}$ ,  $^{87}\text{Sr}/^{86}\text{Sr}$ ,  $^{36}\text{Cl}/\text{Cl}$  and  $\delta^{234}\text{U}$ . Garcia et al. (2021) used  $^{234}\text{U}/^{238}\text{U}$ ,  $\delta^{11}\text{B}$ , and  $^{87}\text{Sr}/^{86}\text{Sr}$  to show how seasonal discharge patterns affect water quality and heterogeneity in a 200-km stretch of river south of Elephant Butte Reservoir over several years. They observed the presence of inputs of geologic and anthropogenic origin to the Rio Grande and the irrigation drain network during non-irrigation (baseflow) conditions, contrasted with relative chemical homogeneity reflective of headwater chemistry during the irrigation/runoff season. Hiebling et al. (2018) evaluated the relationship between water quality and basin structure in the Mesilla Basin, using  $\text{Cl}/\text{Br}$  ratios in conjunction with geophysical data to demonstrate that salinization trends in the Mesilla basin were primarily due to evaporite dissolution rather than upwelling brine.

This work focused on the riverside irrigation drains and the Rio Grande. The drains were installed to lower the water table in the Rio Grande valley, and as such flow in the irrigation drains is an expression of the water table. The riverside drains are typically the lowest points in the valley, frequently lower than the Rio Grande itself. Thus, the drains reflect the riparian aquifer conditions, allowing easy sampling of groundwater without the complication of surface runoff. During irrigation season, cumulative discharge in the riverside drain network can be greater than discharge of the Rio Grande. As such, they are an important hydrologic resource. Sampling of the Rio Grande was also performed in thoroughly characterize the system. Flow in the Rio Grande is volumetrically and chemically transient due to the variability of the sources contributing to flow. The Rio Grande is the primary source of recharge to the riparian aquifer (S.S Papadopoulos & Associates, 2000). Recharge from the river enters the system by direct infiltration from the channel as well as in the form of irrigation return flows. Irrigation water is diverted from the river near the northern extent of the project area, thus the northmost river samples are characteristic of the chemistry of the water entering the system. The Rio Grande is the primary pathway by which water exits the Albuquerque Basin, and so the southernmost river samples integrate basin-scale mixing processes.

Six sites were established longitudinally across the southernmost subbasin of the greater Albuquerque Basin in order to capture the spatial variability of inflow sources and flux rates. Five measurement campaigns were executed throughout the course of the 2021 calendar year to capture seasonal variability. Differential flow gauging was performed in riverside irrigation drains, and drain and river water was analyzed for major and minor anions and cations, trace metals,  $^{87}\text{Sr}/^{86}\text{Sr}$ ,  $\delta^{18}\text{O}$ ,  $\delta^2\text{H}$ ,  $^{222}\text{Rn}$  activity, and field parameters. Trends in water quality were captured in the overall chemistry. Mixing analysis was performed using strontium isotope mass-balance calculations. Inflow rates and trends in volumetric flow were determined from flow gauging and analysis of  $^{222}\text{Rn}$ .

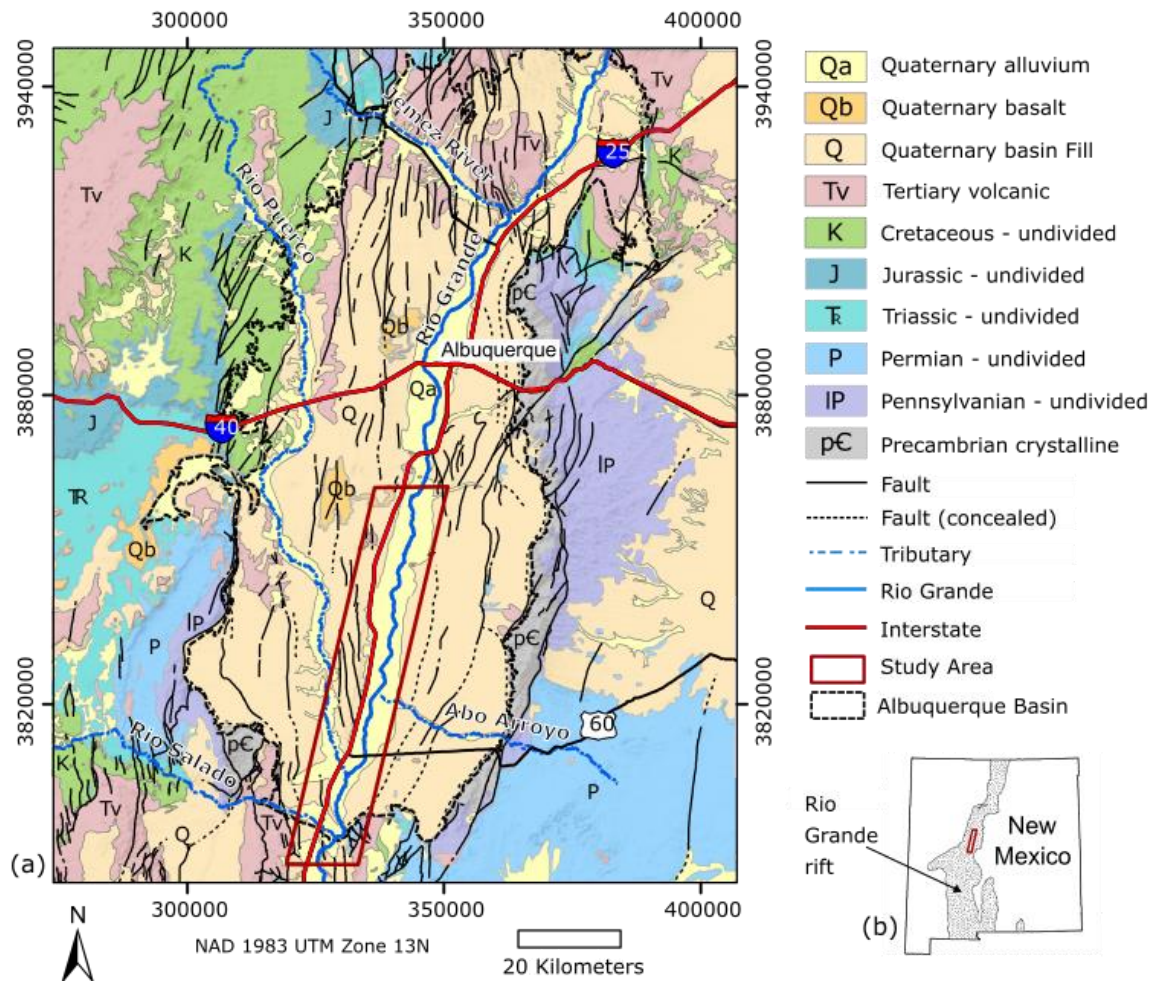


Figure 1.1. Overview of the project area and the regional geologic setting. (a) shows the location of the Albuquerque basin and the geology of the simplified area (simplified from the 1:500,000 New Mexico State Geologic Map). (b) shows the location of the project area and the Rio Grande Rift in reference to the state of New Mexico.

## 1.2 Background

### 1.2.1 Project Area Overview

The Albuquerque basin is a part of the Rio Grande Rift (Fig. 1b), a Cenozoic extensional feature comprised of series of north-south oriented grabens spanning from south-central Colorado through southern New Mexico (Grauch and Connell, 2013). The rift is bounded by the Colorado Plateau to the West, the Great Plains to the East, the Basin and Range to the South and Southwest, and the Rocky Mountains to the North and Northeast. The Albuquerque basin is approximately 8,000 km<sup>2</sup>. The eastern edge of the basin is bounded by uplifted Proterozoic granitic rocks of the Sandia, Manzanita, Manzano, and Los Pinos mountains. Mesozoic and Paleozoic sedimentary rocks of the Colorado Plateau are exposed on the basin's western flank. Neogene-Quaternary volcanic rocks of the Jemez Mountains define the basin's northern extent (Plummer et al., 2004). The Rio Grande travels through the basin from the northeast to the south, carving out a prominent river valley up to about 10-km wide.

The Rio Grande valley hosts most of the the basin's agriculture, as well as a narrow corridor of deciduous forest that borders the river. Sparsely vegetated alluvial fans cover most of the basin's area. Intermittent basaltic volcanoes and lava flows are present throughout the basin. Average annual precipitation in the Albuquerque area since 1971 is 227.3 mm (8.95 in), Temperature ranges from an average high of 38°C (100°F) in June/July to an average low of -11°C (12°F) (in December/January (U.S. National Weather Service). Temperature, precipitation, and evapotranspiration are variable throughout the basin due to differences in elevation, latitude, topography, and land use.

Albuquerque is the largest city in New Mexico with a population of over 560,000 (U.S. Census, 2020) and is located in the middle of the basin along the eastern edge. Rio Rancho is the second largest city in the basin (population ~104,000) and is located immediately to the northwest of Albuquerque. Other major cities in the basin include Bernalillo, Los Lunas, and Belen. Each are located along the river with populations of less than 10,000. Albuquerque is the greatest water user in the basin outside of irrigated agriculture. Until 2008, Albuquerque's  $1.23 \times 10^8$  m<sup>3</sup> (~100,000 ac-ft) annually used water came exclusively from groundwater pumping. It has since begun using surface water (some of which is diverted from the upper Colorado River basin as a part of the San Juan-Chama project) reducing the need to pump groundwater. In 2015, only  $4.93 \times 10^7$  m<sup>3</sup> (40,000 ac-ft) was pumped. (ABCWA, 2020). As shown in Figure 1.5, the proportion of groundwater to surface water used is variable throughout the year and much of the water used is treated and returned to the river.

Irrigation in the Middle Rio Grande is managed by the Middle Rio Grande Conservancy District (MRGCD) which manages surface water deliveries to approximately 239 km<sup>2</sup> (59,000 acres) of farmland using a network of 1,854 km (1,152 miles) of irrigation canals (MRGCD, 2022). Water from the Rio Grande is diverted into the canal network and allocated to farmers for flood irrigation, a practice that has been ongoing since prior to the arrival of the Spanish in the 1500s (Nelson et al., 1914). Alfalfa is the primary agricultural product. Groundwater pumping supplements river diversions: however groundwater pumping is not as extensive along the Middle Rio Grande as the upper and lower reaches.



In 2015, only 6% of irrigation water used in Valencia County (which is encompassed by the project area) came from pumped groundwater (Magnuson et al., 2019). The natural water table in the valley only 58 cm (23 inches) below land surface, which leads to salt accumulation and root waterlogging (Nelson et al., 1914). To combat this, a network of irrigation drains was installed to lower the water table to a depth of several feet. The drain network consists of riverside drains and interior drains: riverside drains are adjacent to the Rio Grande and are typically dug deeper than the depth of the main channel. As such the riverside drains serve as the regional groundwater sink. The riverside drains flow perennially, even when the main river channel is dry. Interior drains are shallower and are distributed throughout irrigated areas, serving to enhance drainage during irrigation season and are often dry outside of irrigation season. Water that accumulates in the interior drains is routed into riverside drains, which in turn are intermittently routed into the river.

MRGCD gauge records indicate that over  $1.31 \times 10^8 \text{ m}^3$  (106,000 acre-feet) of water was diverted in 2021 into the Belen District irrigation network, which extends between Isleta and San Acacia, coincident with the study area. This water was applied to approximately  $121.8 \text{ km}^3$  (30,100 acres) of farmland using ~813 km (505 mile) of delivery ditches (MRGCD, 2022). Additional water pumped from the aquifer is applied to the surface as well. Irrigation water is either lost to evapotranspiration or infiltrates through the soil and into the groundwater system. We refer to waters of the latter case as irrigation return flows. Interactions between irrigation return flows, the soils they infiltrate through, and shallow aquifer sediments leads to the evolution of the return flow water chemistry.

### ***1.2.2 Regional Geology***

The Albuquerque basin is subdivided by the Santa Domingo, Calabacillas, and Belen Subbasins. The subbasins are predominantly easterly tilted half-grabens that are separated by transition zones that segment the basin from north to south (Grauch and Connell, 2013). The basin fill is dominated by the siliciclastic Santa Fe Group (Grauch and Connell, 2013). Active extension in the Albuquerque basin is slowly continuing today at strain rates of  $3.9 \times 10^{-17} \pm 6.3 \times 10^{-18}$  to  $4.4 \times 10^{-17} \pm 6.3 \times 10^{-18} \text{ s}^{-1}$  or at 1.2 mm/yr (Ricketts et al., 2014).

Our study area is in the Belen subbasin (Fig. 1.2), the largest of the three subbasins at 40 km wide, 60 km long, and 4 km deep. It is separated from the Calabacillas subbasin to the north by the Mountainview Prong, a NW-SW trending antiform (Grauch and Connell, 2013). The Manzano and Los Pinos Mountains bound the eastern edge of the basin, and the Lucero uplift and Sierra Ladrones (both comprised of Paleozoic and Mesozoic strata) define the western extent. To the south, the Albuquerque basin transitions into the Socorro basin through the Socorro (or San Acacia) constriction, a roughly 10-mile wide structural high that is bounded to the west and east by the Ladron and Joyita uplifts (Plummer et al., 2004; Roybal, 1991).

The rift fill of the Santa Fe Group in the Belen subbasin consists of the Popatosa Formation (piedmont and fluviolacustrine conglomerate, mudstone, and sandstone), Arroyo Ojito Formation (mixed eolian/fluviol to mud/gravel fluvial), and Sierra Ladrones Formation (course fluvial and piedmont deposits) from bottom to top respectively (Connell, 2001). All of these formations are heterolithic, and clast proportions vary with

respect to source proximity. Clasts are derived from sources including: the Paleozoic-Mesozoic sedimentary section exposed in the Colorado Plateau to the northwest, the Lucero uplift and Sierra Ladrones to the southwest, and the Los Pinos mountains to the southeast; basaltic-rhyolitic volcanic rocks of the Mogollon-Datil volcanic field, Jemez Mountains, intra-rift intrusive and extrusive mafic rocks; and Proterozoic plutonic rocks exposed in the cores of the Sandia, Manzano, and Manzanita mountains to the East, the Los Pinos mountains to the southeast, and the Sierra Ladrones to the southwest (Fig. 1.1; Fig 1.2). Clays in the Santa Fe Group are dominantly 2:1 clay minerals (Gillentine, 1996).

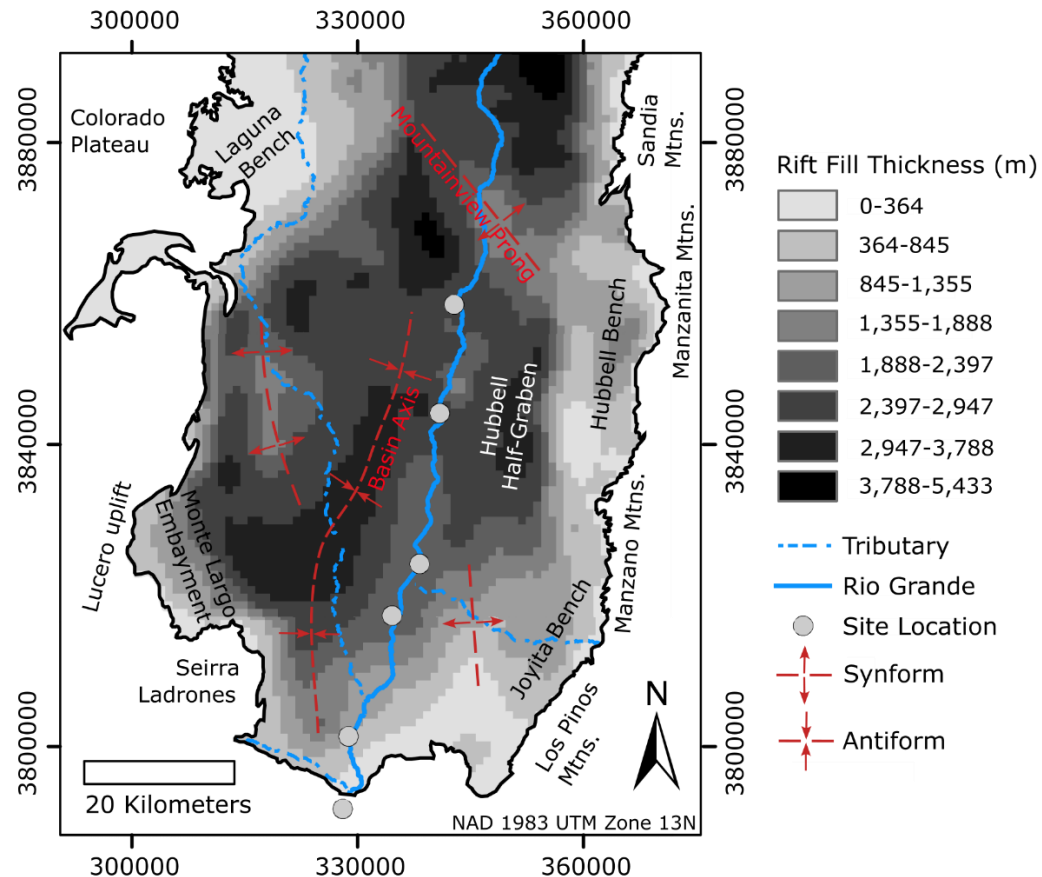


Figure 1.2. Rift fill thickness within the Southern Albuquerque Basin (Grauch and Connell, 2013) showing site locations, the Rio Grande and major tributaries, and physiographic and structural features.

Soils in the valley have dominantly loamy textures and have higher Sodium Adsorption Ratios (SAR) and surface salt concentrations in the southern end of the project area (Fig. 2.2), particularly south of the confluence of the Rio Puerco. SAR is a measure of soil sodicity – or the ratio of sodium to calcium and magnesium. The SAR distribution is of particular interest insofar as it may be indicative of ion exchange conditions resulting in the observed change in Na/Ca of phreatic waters along flow distance in this study (Essington, 2004). The average composition of surficial salts is approximately 10 parts sodium-sulphate, 4 parts sodium-chloride, 2 parts gypsum, and one part magnesium-chloride (Nelson et al., 1914).

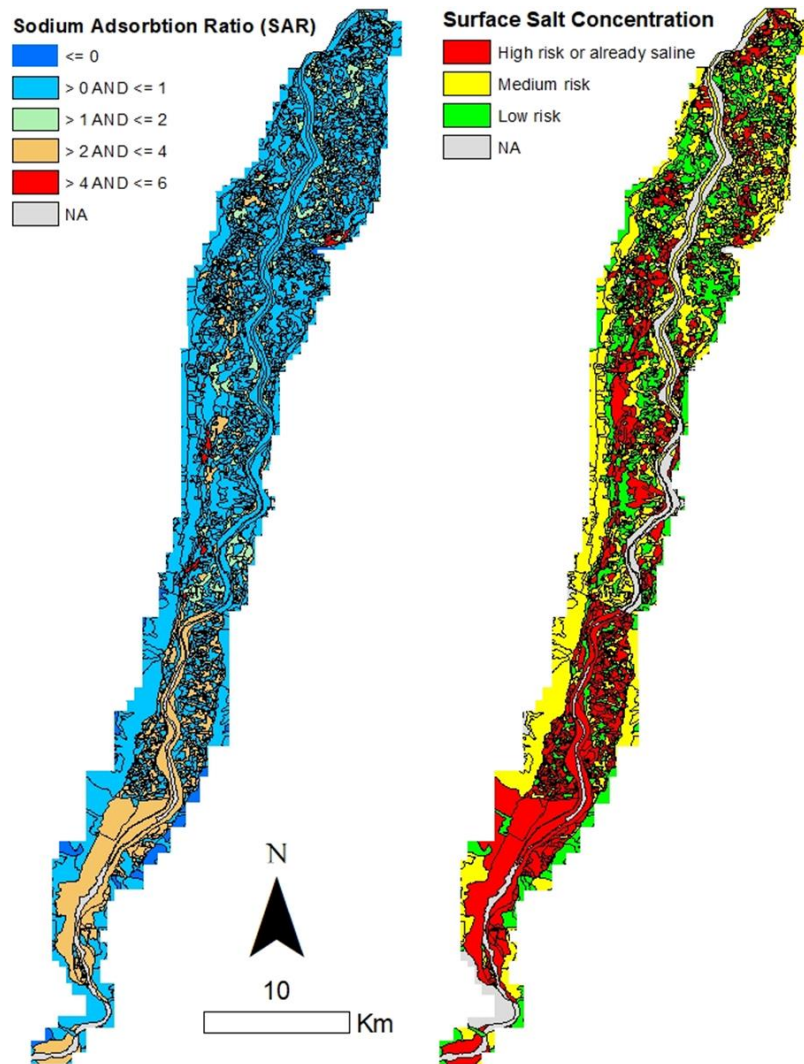


Figure 1.3. Soil Surface Salt Concentration and SAR in the MRGCD Belen District. Data from NRCS SSURGO Database accessed and displayed in ArcMap

### 1.2.3 Hydrology

The Rio Grande originates in the San Juan Mountains of southwest Colorado and flows south through New Mexico, subsequently defining the boundary between Texas and Mexico before terminating into the Gulf of Mexico. The majority of the river's flow is derived from spring runoff of headwaters snowpack and is supplemented by summer monsoon rains. Discharge generally decreases along its 3,060 km (1900 mi) path due to evapotranspiration (ET), infiltration, and consumptive withdrawals. By convention, the river is considered in upper, middle, and lower segments – the middle segment falling between Otowi, NM and Elephant Butte Reservoir. A combination of groundwater withdrawal and streambed aggradation has created or exacerbated negative hydrologic gradients out of the river in the majority of the Middle Rio Grande. However gaining reaches of river exist, such in as the southern Albuquerque basin (Bexfield and Anderholm, 2000; S.S Papadopoulos & Associates, 2000)

The hydrogeology of the Albuquerque basin has been extensively studied relative to other basins of the Rio Grande Rift. Plummer et al. (2004) synthesized available data to create a thorough hydrogeochemical characterization of the basin, in which he identified 12 hydrogeochemically distinct zones of groundwater, defined groundwater age gradients and recharge timing, and characterized physical aspects of groundwater flow (Fig. 2.3). Sources of water to the basin include: inflow from the Rio Grande and its tributaries (e.g. Jemez Creek, Rio Puerco, Abo Arroyo, and Rio Salado); mountain front recharge from the Sierra Ladrones and Jemez, Sandia, Manzanita, Manzano, and Los Pinos Mountains; inflow of saline groundwater in the southwest basin margin; and local precipitation during summer monsoons (Plummer et al., 2004). Sinks include evapotranspiration, anthropogenic consumptive use, Rio Grande outflow, and possible groundwater infiltration to surrounding aquifers. The outlet of the Albuquerque basin at San Acacia integrates a ~72,200 km<sup>2</sup> watershed, without considering the watershed area contributed by the San Juan – Chama project. The median radiocarbon ages of major groundwater zones are between 3,000 and 20,000 years old and some samples measured greater than 30,000 years old – however deep basin flows may be millions of years old (Plummer et al., 2004; Williams et al., 2013).

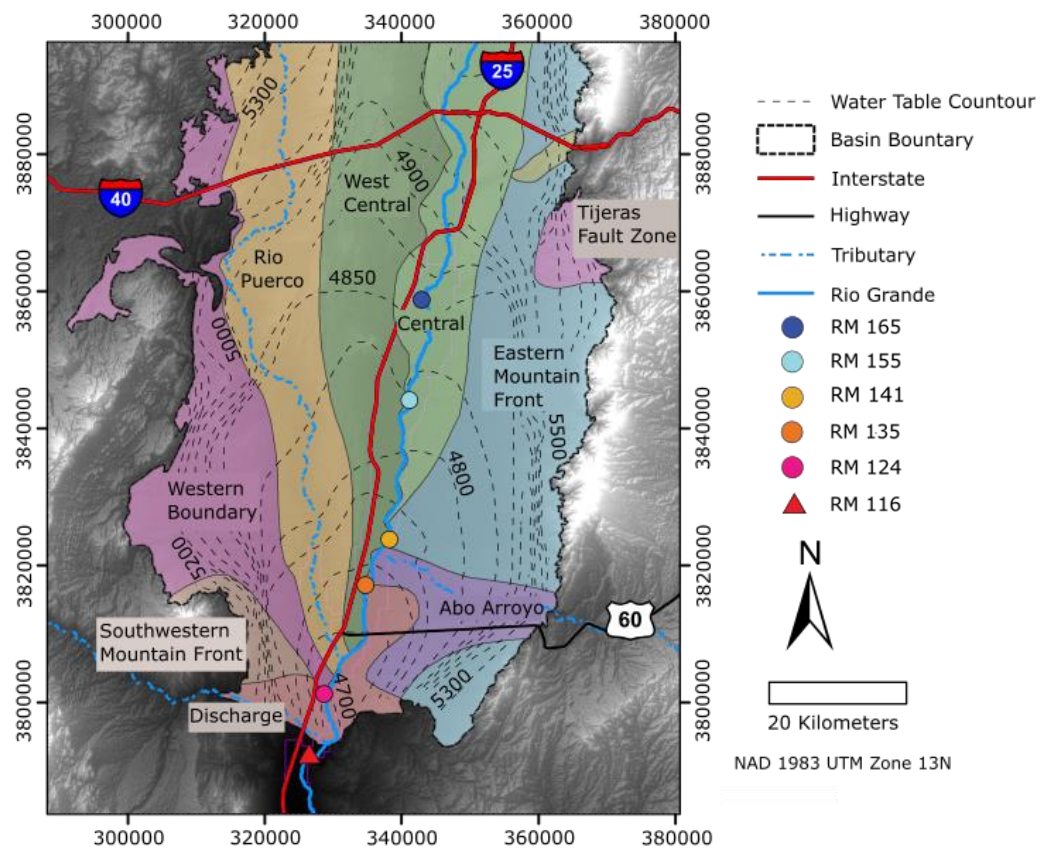


Figure 1.4. Hydrogeochemical groundwater zones (Plummer et al., 2004) and predevelopment groundwater contours (Bexfield and Anderholm, 2000) of the Southern Albuquerque basin. Contours are in 25-meter intervals.

#### ***1.2.4 2021 Rio Grande Flow History***

Flow through the Rio Grande was highly variable throughout 2021 (Fig. 1.4a). Four gauges maintained by the USGS exist in the project area. The northern gauge is near the town of Bosque Farms, approximately 166 river miles (RM) above Elephant Butte Reservoir (The river mile reference convention is used by the USBR and other management agencies. River mile distance considers the sinusoidal path of the river, not straight-line distance. Higher river mile (RM) values are further upstream (north), and vice versa.). The Bosque gauge is near RM 141, the Bernardo Gauge at RM 130, and the San Acacia Gauge at RM 116. Between January and late March flows at all gages in the project area ranged from 12.7-18.4 m<sup>3</sup>/s (450-650 CFS). San Acacia typically had the highest discharge in this period, followed by Bosque, Bosque Farms, and Bernardo. From late March to May average conditions were variable but consistent between gauges, with average flows ranging from 5.7-36.8 m<sup>3</sup>/s (200-1300 CFS). Bosque farms typically had the highest discharge in this period, followed by Bosque, San Acacia, and Bernardo. Peak runoff occurred in early May. From June through September flow became highly variable and inconsistent between gauges due to a combination of irrigation diversions and monsoon rains. Discharge ranged from almost 56.6 m<sup>3</sup>/s (2000 CFS ) at San Acacia to zero flow at Bernardo, where the river intermittently dried. Flow gradually increased overall from October to the end of the year, once again becoming consistent between gauges. Flow ranged from 2.8-28.3 m<sup>3</sup>/s (100-1000 CFS) at the end of the year, mirroring the early year conditions with slightly more variability.

Tributary inflow from Jemez River, Abo Arroyo, the Rio Puerco, and Rio Salado driven by monsoon precipitation contributed to the variability in Rio Grande flow during the summer. A remaining major tributary is discharge from the Albuquerque Bernalillo County Water Authority (ABCWA) Wastewater Treatment Plant. This source is immediately north of the project area and discharges at a consistent rate of ~1.1 m<sup>3</sup>/s throughout the year, however the chemistry of the water from this source depends on the source of water used by the city – either water diverted from the Rio Grande or groundwater pumped from the city's wells. When river flows are low, most or all of the water used by Albuquerque comes from groundwater. The proportion of river water to groundwater used by Albuquerque throughout the year is shown in Figure 1.4(a). During much of the summer, discharge from the treatment plant is the primary source of flow to the project area.

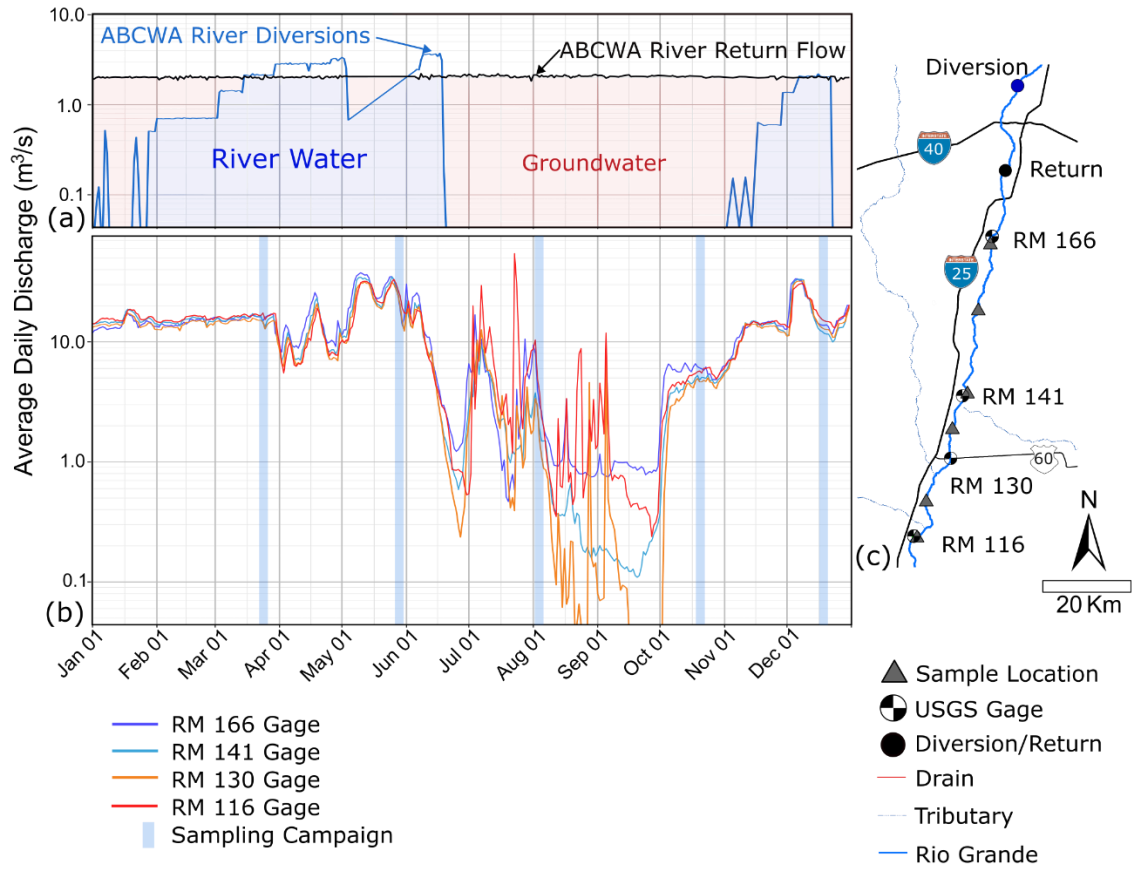


Figure 1.5: (a) 2021 surface water diversions/returns made by the Albuquerque Bernalillo County Water Authority (ABCWA). (b) 2021 Rio Grande discharge records from USGS gages in the project area. (c) Schematic map showing sample locations, USGS gages, and ABCWA river diversion and return locations.

## CHAPTER 2

### METHODS

#### 2.1 Site descriptions and overview

Five sampling campaigns were performed in 2021 in the months of March, May, August, October, and December (Fig. 1.5). During each campaign, water samples were collected from the Rio Grande main channel and adjacent riverside drains between Bosque Farms and San Acacia, at approximately 165, 155, 141, 135, 124, and 116 river miles (RM) above Elephant Butte Reservoir (Fig. 3.1). No drain samples were collected at San Acacia (RM 116). Water samples were analyzed for a suite of geochemical constituents, including major and minor anions and cations, trace metals,  $^{87}\text{Sr}/^{86}\text{Sr}$ ,  $\delta^{18}\text{O}$ , and  $\delta^2\text{H}$ . Field parameters including pH, TDS, specific conductivity, temperature, and dissolved oxygen were measured in site during sample collection with a YSI EXO1 multiprobe. All the geochemical constituents were measured in all samples collected excluding  $^{87}\text{Sr}/^{86}\text{Sr}$ , which was only analyzed in the riverside drains and the river at RMs 165 and 116. Differential flow gauging and sample collection in the riverside drains were done at the same time. For differential flow gauging, we used a conventional flow meter as well as dilution gauging with rhodamine dye. Quantitative provenance analysis was performed using solute and isotope mass balance equations of  $^{87}\text{Sr}/^{86}\text{Sr}$  and  $\text{Sr}^{2+}$  concentrations using endmember data obtained from Hogan et al. (2007), Burke et al. (1982), Williams et al. (2013), Plummer et al. (2004), and Mukhopadhyay and Brookins (1976).

##### 2.1.1 RM 165: Bosque Farms

The Bosque Farms site is the northernmost sampling location. It is in the Upper Peralta Riverside Drain on the eastern side of the river adjacent to river mile 165, immediately across from the end of Cottonwood Drive in Bosque Farms. The sample location is approximately 383 m from the center of the Rio Grande main channel and is approximately 2 m lower in elevation than the Rio Grande channel. There are 5.8 km of upstream drain from the sample collection point. Samples were collected downstream of an earthen bridge over steel culvert through which flow was continuous without a hydraulic jump. Land use immediately around the site is a mixture of residential and agricultural.

The RM165 drain generally had low turbidity. The drain's bank is reinforced by igneous boulders, and the bed was primarily sandy except in the vicinity of the bridge and culvert where mud, silt, and organic matter had accumulated. Vegetation (mostly parrot-



feather) was seasonally abundant, particularly near the bridge and culvert. However, the vegetation thinned over the course of the year.

### **2.1.2 RM 155: Tome**

The Tome Drain site is located within the Lower Peralta Riverside Drain on the eastern side of the river approximately adjacent to river mile 155. The sample location is approximately 175 m from the center of the Rio Grande main channel, and approximately 2 m lower in elevation than the riverbed. 29.6 km of drain are upstream of the sample location, and the upstream network includes the Upper Peralta Riverside Drain (where the RM 165 drain is located) as well as interior drains. This site is accessible from Silva Road to the east and from the MRGCD access road on the west.

This drain has a particularly high and steep levy composed of finer sediment. The bed is mostly sandy and flat. Parrot-feather in the channel can be locally extensive, but sufficiently clear areas that accommodated measurement were readily encountered. Tamarisk grew densely along the much of the bank. This reach of drain is curved, with the concave portion to the West. Land use adjacent to this site is predominantly agricultural

### **2.1.3 RM 141: Bosque**

The Bosque drain site is located within the Upper San Juan Riverside Drain on the eastern side of the river near river mile 134. The sample location is 185 m from the Rio Grande main channel midpoint and approximately 1 m below the riverbed. 7.8 km of drain network is upstream of this location. The site is directly above NM State Highway 346 and is easily accessible. The Bosque USGS gauge is co-located with the Hwy. 346 bridge. The immediate area is primarily agricultural (mostly alfalfa farming). A large dairy with a center pivot sprinkler and multiple large effluent ponds is approximately 2 km to the east.

This drain was typically quite stagnant near the sample location, which was a short distance upstream from where the drain passed through a culvert under the highway. In this location, parrot-feather and small bright green floating aquatic plants were variably abundant and the bed was composed of deep organic rich mud. Turbidity was low. Trapped dissolved gas in this mud would become released when disturbed. Upstream, flow velocity was higher and readily apparent, and the bed was sandy. Cattails and parrotfeather were abundant here. A fire in the Bosque between the site and the river occurred here between the May and August campaign, charring trees, However, the drain itself was not affected.

### **2.1.4 RM 135: Abeytas**

The Abeytas drain site is on the western side of the river near river mile 151 in Drain No. 7. The sample location is approximately 300 meters from the center of the Rio Grande channel and at similar elevation to the river. There is 70.6 km of upstream drain network above the sample location. This drain splits immediately below the site, where most of the flow is diverted into the San Francisco Riverside drain and some flow passes over a boulder dam into the Bernardo Interior Drain. A hydraulic jump of several meters occurs at this junction. Land is mostly barren in the immediate vicinity, with some residential and agricultural property. A small dairy between New Mexico State Highway 116 and Interstate 25 is located to the west. A railway parallels the western edge of the



drain. The site is accessible from the town of Abeytas following MRGCD access roads. The bed at this site is a mixture of sand, silt, and mud, and flow was fairly turbid. Tamarisk was extensive along the banks, although it was mowed halfway through the year. The bank is fairly low and comprised of native soil. Flow undercut the bank by up to half a meter, but the bank remained stable due to vegetation.

### **2.1.5 RM 124: La Joya**

The La Joya drain site is in the Unit No. 7 Drain on the western side of the river adjacent to river mile 124. The site is 275 m from the center of the Rio Grande main channel and at approximately equal elevation to the river. 120.6 km of drain network contributes to this site. This drain is accessible by crossing briefly through the Sevilleta National Wildlife Refuge, which in that area is open to the public. The site itself is within the La Joya Waterfowl Management Area of the Ladd S. Gordon Waterfowl Complex, which has 600 acres (2.4 km<sup>2</sup>) of man-made ponds that provide habitat to migrating birds. The ponds are filled seasonally to accommodate migrating waterfowl. Some of these ponds are to the west of the site, on the other side of a railway and an interior drain. This drain has an engineered cobble to boulder bed and has several engineered hydraulic jumps. The Unit No. 7 drain is also sometimes used to convey irrigation water.

### **2.1.6 RM 116: San Acacia**

The San Acacia site is in the Rio Grande itself at the San Acacia Diversion Weir at river mile 116. A complicated network of diversion structures is used to route water between the Unit No. 7 Drain (which here is located significantly higher than the river), the Socorro Main Conveyance Channel, and the Rio Grande Main channel. The Low Flow Conveyance Channel begins at the weir. The San Acacia USGS gauge is located downstream of the diversion structures. Samples were collected upstream of the weir and diversion structures. Upstream of the dam suspended sediment was fine and very abundant, but downstream the riverbed was composed of sand to boulder sized clasts. A basalt vent and saline spring system are situated immediately to the west of the site, which contribute to the hydrologic complexity of the site. Williams et al. (2013) showed that the salt spring system is partially fed by ascending mantle fluids that may also flow into the river (Williams et al., 2013).

## **2.2 Flow Gauging**

### **2.2.1 Differential Flow Gauging**

Differential flow gauging was performed in drains using conventional and dilution methods. Differential flow gauging is a simple means of determining groundwater flux, where the groundwater flux is equal to the difference between the downstream and upstream discharge divided by the interval between measurements. Measurement intervals ranged from 188 to 800 meters. Greater spacing was used for sites with higher flow volumes. Conventional flow measurements were done using a Hach model FH950.0 flow meter and wading rod following standard methods (International Organization for Standardization, 2021). Average velocity ( $\bar{v}$ ) was taken using the one-point method, which assumes the average velocity is approximately equal to the velocity at 0.6 of the total depth ( $d$ ) below surface. Measurements were collected at 1 ft (0.3 m) intervals across the channel width. Total discharge ( $Q$ ) was calculated using the mid-section method (equation 1):

$$Q = \sum_{n=1}^m \overline{v_n} d_n \left( \frac{b_{n+1} - b_{n-1}}{2} \right) \quad (1)$$

where  $n$  is the measurement number,  $m$  is the number of measurements, and  $b$  is the distance of a measurement from the bank (ISO 748, 2022).

Dilution flow gauging was performed by injecting a slug of rhodamine wt dye following Kilpatrick and Cobb (1985). The concentration of the dye slug was measured in situ at 10 second intervals using Turner C3 fluorometers, which have rhodamine wt specific optical sensors and automatically compensates for changes in fluorescence due to temperature changes. The sensors were calibrated prior to deployment. Dye was injected at a sufficient distance upstream of the first fluorometer for complete longitudinal mixing to occur, typically several hundred meters to over a kilometer. The fluorometers were installed in the channel at the same approximate location as manual gauging was performed. Discharge was determined by dividing the mass of dye injected by the area of the time concentration curve recorded by each fluorometer using formula (2) where  $S_G$  is the dye's specific gravity,  $V_I$  is the volume of dye injected ( $L^3$ ),  $C$  is the concentration of the dye ( $M/L^3$ ), and  $A_c$  is the area under the time concentration curve ( $M \cdot T/L^3$ ).

$$Q = \frac{S_G V_I C}{A_c} \quad (2)$$

### 2.2.2 Estimating Inflow Rate from Radon Activity

The groundwater inflow rate was estimated based on the difference between the average  $^{222}\text{Rn}$  activity of groundwater and the  $^{222}\text{Rn}$  activity of the channel water.  $^{222}\text{Rn}$  is a member of the uranium-238 decay series with a half-life of 3.8 days,  $^{222}\text{Rn}$  is continuously produced within the aquifer by uranium bearing minerals, which are commonly associated with granitic sediments (Clark, 2015) which are a major constituent of Albuquerque basin fill (Section 1.2.2). Groundwater discharge contributes  $^{222}\text{Rn}$  to streams, where  $^{222}\text{Rn}$  activity subsequently decreases due to gas exchange and radioactive decay. The mass balance for radon in a channel is given in Equation 3, where  $Q$  is stream discharge ( $L^3/T$ ),  $x$  is distance,  $c$  is the radon activity of the stream water (activity/ $L^3$ ),  $I$  is groundwater inflow ( $L^3/T/L$ ),  $c_i$  is the radon activity of groundwater inflow ( $\{^{222}\text{Rn}\}/L^3$ ),  $k$  is the gas transfer velocity ( $L/T$ ),  $w$  is the average river width ( $L$ ),  $c_a$  is the radon concentration of air-equilibrated water ( $\{^{222}\text{R}\}/L^3$ ),  $\lambda$  is the radioactive decay coefficient ( $T^{-1}$ ), and  $d$  is the average stream depth ( $L$ ) (Cook, 2013). Assuming steady state flow and a negligible concentration of radon in air-equilibrated water, Equation 3 may be simplified and rearranged to Equation 4. Groundwater inflow ( $m^3/d/m$ ) was calculated with Equation 4 using the average channel dimensions measured during conventional flow gauging and an estimated gas transfer velocity of 1.0 m/d, which is a typical value for low gradient river (Cook et al., 2003).

$$\frac{\partial Qc}{\partial x} = Ic_i - kw(c - c_a) - \lambda dwc \quad (3)$$

$$I = \frac{cw(k+\lambda d)}{c_i} \quad (4)$$

The  $^{222}\text{Rn}$  dissolved gas activity in the channel was measured using a Durrige RAD7 Electronic Radon detector. During the March and May campaigns  $^{222}\text{Rn}$  was measured in the field by pumping water from the channel through a Durrige RAD AQUA degassing apparatus and measuring the  $^{222}\text{Rn}$  concentration of water equilibrated air at 5-minute intervals over a 1-to-2-hour period. Midway through the August campaign, the RAD7 malfunctioned and required maintenance and only two sites were measured. Subsequent  $^{222}\text{Rn}$  measurements from the October and December campaigns were collected in the field and analyzed in the lab using the RAD7 WAT250 protocol (Durrige, 2020). Samples for radon analysis were collected synchronous to other water samples in 250-ml zero-headspace bottles. The bottles were filled underwater using a peristaltic pump to eliminate contact between the sample and the atmosphere. Samples from two wells in the project area were analyzed for  $^{222}\text{Rn}$  using this method and averaged to provide the  $c_i$  parameter (2.45 Bq/l).

### 2.3 Water Sampling and Analysis

Water samples were collected from the drains and river into acid-washed 250ml and 120-ml HDPE bottles using a ‘Montana style’ peristaltic pump (Woessner, 2007) and an inline 0.45-micron filter. Samples for trace metal and  $^{87}\text{Sr}/^{86}\text{Sr}$  analysis were acidified using trace metal grade nitric acid.  $\delta^{18}\text{O}$  and  $\delta^2\text{H}$  samples were collected in glass no-headspace vials directly from the channel. Samples were refrigerated upon collection until analysis. In some instances, flow in the Rio Grande was too turbid to effectively filter in the field. In those cases, grab samples were collected directly from the river and were frozen prior to filtration in the laboratory.

Cations, anions, trace metals, and the isotopic composition ( $\delta^{18}\text{O}$  and  $\delta^2\text{H}$ ) of samples were analyzed in the New Mexico Bureau of Geology Analytical Chemistry Laboratory using EPA methods 200.7, 300.0, 200.8 and a Picarro isotope analyzer respectively.  $^{87}\text{Sr}/^{86}\text{Sr}$  analysis was conducted at the University of Texas at El Paso with a Nu Plasma HR multi-collector ICP-MS following the procedure described by Garcia (2021).

### 2.4 Geochemical Analysis

Geochemical trends and mixing behavior was observed by changes in solute load over distance,  $\delta^{18}\text{O}$  vs.  $\delta^2\text{H}$ ,  $(\text{CO}_3^{2-} + \text{HCO}_3^-)$  vs.  $(\text{SO}_4^{2-} + \text{Cl}^-)$  vs.  $(\text{Ca}^{2+} + \text{Mg}^{2+})$  vs.  $(\text{Na}^+ + \text{K}^+)$ , as well as  $^{87}\text{Sr}/^{86}\text{Sr}$  and  $\text{Sr}^{2+}$  solute and isotope mass balance equations. Evaporation was evaluated using a  $\delta^{18}\text{O}$  Rayleigh distillation model. Chemical variability was compared against spatial distribution and the composition of potential endmembers, such as groundwaters from hydrogeochemical zones identified by Plummer et al. (2004) and deep basin brine (Hogan et al., 2007; Williams et al., 2013).

### 2.4.1 Saturation Indices

Mineral saturation indices (SI) were calculated using Geochemist's Workbench (GWB) Community Edition (version 15.0.1, 2021). Sample data from each campaign at each site was inputted into the 'Geochemist's Spreadsheet' – a subprogram of GWB which calculates the SI of specified minerals in terms of  $\log(Q/K)$ , where  $Q$  is the activity product and  $K$  is the equilibrium constant for the precipitation/dissolution reaction for a particular mineral. When  $\log(Q/K)=0$ , a mineral is at equilibrium with the solution.  $\log(Q/K)>0$  indicates a mineral is supersaturated, and vice versa. The input parameters included TDS (mg/kg), carbonate alkalinity (mg/kg as  $\text{CaCO}_3$ ), and EC ( $\mu\text{S}/\text{cm}$ ), as well as the following selected ions:  $\text{Mg}^{2+}$ ,  $\text{Na}^+$ ,  $\text{K}^+$ ,  $\text{HCO}_3^-$ ,  $\text{SO}_4^{2-}$ ,  $\text{Cl}^-$ ,  $\text{Ca}^{2+}$ ,  $\text{F}^-$ ,  $\text{SiO}_3$ ,  $\text{Al}^{3+}$ ,  $\text{Ba}^{2+}$ ,  $\text{Li}^+$ , and  $\text{Sr}^{2+}$ . These were used to calculate the SI of the following minerals at each site during each campaign: albite, anorthite, barite, brucite, calcite, dolomite, illite, kaolinite, muscovite, and quartz.

### 2.4.2 Evaporation

The degree of drain water evaporation was determined using a  $\delta^{18}\text{O}$  Rayleigh distillation model. Analysis was performed on the drains and the river, using the  $\delta^{18}\text{O}$  value from the river and drain at RM 165 as the source water of the river and drain respectively for a given month. The simplified formula is given in Equation 5, where  $f$  is the fraction of the sample lost to evaporation and  $E$  is the kinetic enrichment factor of  $\delta^{18}\text{O}_w - \delta^{18}\text{O}_v$ . The appropriate enrichment factor depends on the relative humidity (RH) in the system, which is determined by the slope of the sample data. A slope of 6 corresponds to a RH of ~80% and an  $E$  of 12.9, a slope of 5 corresponds to a RH of ~50% and an  $E$  of 16.4, and a slope of 4.2 corresponds to a RH of ~20% and an  $E$  of 19.2 (Clark, 2015).

$$f_{\text{evaporated}} = 1 - e^{(\delta^{18}\text{O}_{\text{final}} - \delta^{18}\text{O}_{\text{initial}})/-E} \quad (5)$$

### 2.4.3 Strontium isotope analysis

Strontium occurs in nature as a divalent cation that behaves similarly to calcium. As such it substitutes isomorphically with calcium in minerals such as calcite and anorthite.  $^{87}\text{Sr}/^{86}\text{Sr}$  is the ratio of radiogenic strontium ( $^{87}\text{Sr}$ ) to stable strontium ( $^{86}\text{Sr}$ ). Radiogenic strontium is produced by the decay of rubidium-87, which has a half-life of  $4.8 \times 10^{10}$  years (Hogan et al., 2000).  $^{87}\text{Sr}/^{86}\text{Sr}$  is stable and does not fractionate during dissolution or precipitation reactions and has distinct values for different geologic materials (Clark, 2015). As such it serves as a powerful indicator of water/rock interactions.

Mixing calculations using solute and isotope mass balance equations of  $^{87}\text{Sr}/^{86}\text{Sr}$  and  $\text{Sr}^{2+}$  concentrations were performed following the procedure for three-component mixing described by Clark (2015). Identifying mixing behavior between endmember waters in a system is done by plotting  $^{87}\text{Sr}/^{86}\text{Sr}$  against  $1/[\text{Sr}]$  – wherein straight mixing lines are formed between endmembers (since  $^{87}\text{Sr}/^{86}\text{Sr}$  is a dependent parameter of  $[\text{Sr}]$  endmember mixing relationships are hyperbolic) (Clark, 2015). The system of equations used to solve for end member fractions is given in equations 6a, 6b, and 6c, where  $M$  is the mass of  $\text{Sr}^{2+}$ ,  $\delta$  = the  $^{87}\text{Sr}/^{86}\text{Sr}$  value, and  $f$  = end member fraction.

$$f_{Paleo} = 1 - f_{Brine} - f_{Rio} \quad (6a)$$

$$f_{Brine} = \frac{M_{Sample} - M_{Rio} - f_{Paleo}(M_{paleo} - M_{Rio})}{M_{Brine} - M_{Rio}} \quad (6b)$$

$$f_{Rio} = \frac{\delta_{Sample} M_{Sample} - \delta_{Brine} M_{Brine} - f_{paleo}(\delta_{Paleo} M_{Paleo} - \delta_{Brine} M_{Brine})}{\delta_{Rio} M_{Rio} - \delta_{Brine} M_{Brine}} \quad (6c)$$

## CHAPTER 3

### RESULTS

#### 3.1 Rates of Groundwater Flux

##### *3.1.1 Overview*

Groundwater flux rates were measured using differential flow gauging and estimated based on the activity of radon. The distance between gauge measurements used to determine flux rates are given in Table 3.1. In many cases, one or more measurements by a given method could not be performed due to site conditions or instrumentation failures. Conventional gauging typically yielded high confidence results, however conventional measurements could sometimes not be performed due to vegetation or flow conditions. In cases where only one conventional flow measurement could be performed at a site, no inflow calculation could be obtained. In some instances, no conventional measurements could be collected at a site, so records of volumetric flow are only available from dilution gauging. An overview of average discharge and inflow rates are provided in Table 4.1.

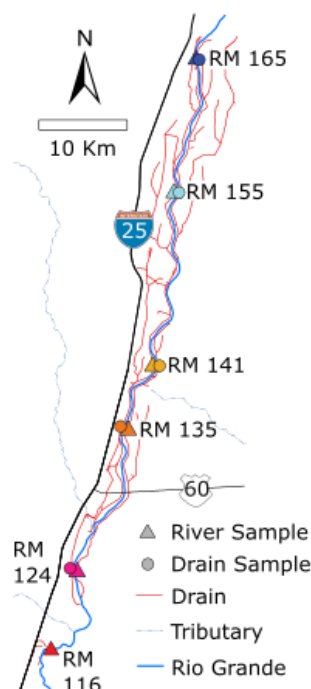


Figure 3.1. Symbol key schematic showing site locations and their river mile designation. The color and shape of the symbols correspond with the subsequent figures.

Drain Site	Upstream drain network length (km)
RM 165	5.8
RM 155	29.6
RM 141	7.8
RM 135	70.6
RM 124	120.6

Table 3.1. Length of upstream drain network above drain site sample locations

### 3.1.2 Radon Inflow

The activity of radon was measured at every site during every campaign, excluding RM 124 in March and RM 165- RM 141 in August due to equipment failure. Radon activity in drain water varied from 0.13 to 2.23 Bq/L (Table 4.1). The radon activity of groundwater from Well #1 was 2.76 Bq/l and Well #2 was 2.14 Bq (average groundwater activity of 2.45 Bq/L). Agreement between the inflow rate estimated by radon activated and the rate calculated from differential gauging was poor. This can be attributed to the fact that the

radon method integrates upstream conditions from a greater upstream area as opposed to a discrete interval. The total upstream length of the contributing drain network to a given site is given in Table 3.1. The amount of length for which a radon inflow estimation is relevant to is a function of the length of the upstream network, average discharge in the network, and the average flow velocity. Radon measurements from the Rio Grande were taken from several locations in May and from all locations in October. Radon activity in the Rio Grande ranged from 0.0 Bq/L to 0.14 Bq/L, averaging 0.05 Bq/l. Inflow rates for the river were not calculated due to the lack of channel geometry and velocity parameters for given river sample sites.

### ***3.1.3 Physical Flow Gauging***

Dilution gauging was performed at every site during every campaign, however unsuccessful deployments occurred on two occasions. In August, floating vegetation became entangled in the downstream fluorometer optics at RM 165, preventing it from accurately measure the passage of the rhodamine wt plume. In October, the data collected from both fluorometers deployed at RM 141 became corrupted during the data export process for unknown reasons. Measurements and calculated inflow rates are presented in Table 3.2. Where the difference between the downstream and upstream discharge measurements ( $\Delta Q$ ) is less than the error (where the error is the sum of each measurement times an assumed error of 5%) the inflow measurement can be assumed to be low confidence. Confidence in the calculated inflow increases with respect to the excess of the inflow relative to the error.

Several significant sources of error were present in the dilution gauging measurements. Mass loss of rhodamine in the channel due to sorption upon suspended sediment, vegetation, and bank materials was a pervasive issue evident by dramatically higher discharge values obtained by dilution gauging vs. manual gauging. Incomplete mass recovery of dye at measurement locations results in a smaller integrated value of the time/concentration curve, resulting in overestimations of flow. Disparity between conventional measurements and dilution measurements was greatest in May and August, when turbidity in the drains was high. Error also arose from variable background fluorescence, debris interference with the fluorometer optics, and the correction factors and integration limits used in the discharge calculations.



Table 3.2. Dilution gauging results. Q=discharge. Error calculation assumes error = 5%.

Drain Site	Month	Spacing (m)	Q upstream (m <sup>3</sup> /s)	Q downstream (m <sup>3</sup> /s)	Avg. Q (m <sup>3</sup> /s)	$\Delta Q$	Error (m <sup>3</sup> /s)	Inflow (m <sup>3</sup> /m/d)
RM 166	March	200	0.3	0.3	0.3	-0.1	0.9	-0.1
	May	384	0.3	0.4	0.4	1.0	1.3	0.6
	August	384	0.3	-	0.3	-	-	-
	October	384	0.4	0.4	0.4	0.0	1.5	0.0
	December	384	0.2	0.2	0.2	0.8	0.7	0.5
RM 155	March	290	1.3	1.2	1.2	-3.7	4.4	-3.1
	May	800	1.9	1.6	1.7	-9.9	6.1	-3.0
	August	800	1.2	1.3	1.3	2.3	4.4	0.7
	October	800	1.4	1.5	1.4	3.0	5.1	0.9
	December	800	1.3	1.4	1.3	2.7	4.7	0.8
RM 141	March	206	0.1	0.2	0.1	3.0	0.5	3.6
	May	206	0.3	0.3	0.3	1.0	1.0	1.1
	August	206	0.1	0.1	0.1	-1.8	0.3	-2.1
	October	206	-	-	-	-	-	-
	December	206	0.1	0.1	0.1	0.2	0.3	0.2
RM 135	March	188	1.0	1.2	1.1	7.6	4.0	9.9
	May	188	2.7	2.6	2.6	-3.9	9.2	-5.0
	August	188	3.7	3.8	3.8	3.5	13.4	4.5
	October	188	2.0	2.1	2.1	2.6	7.3	3.4
	December	188	0.8	0.8	0.8	0.8	2.9	1.1
RM 124	March	200	1.2	1.2	1.2	-0.1	4.2	-0.1
	May	660	4.3	4.2	4.2	-3.8	15.0	-1.4
	August	660	2.8	2.9	2.9	4.6	10.1	1.7
	October	660	1.2	1.3	1.3	2.3	4.4	0.9
	December	660	0.4	0.5	0.4	0.5	1.6	0.2

Table 3.3. Conventional gauging results. Q=discharge. Error calculation assumes error = 5%.

Drain Site	Month	Spacing (m)	Q (m <sup>3</sup> /s) up-stream	Q (m <sup>3</sup> /s) down-stream	Avg. Q (m <sup>3</sup> /s)	$\Delta Q$	Error (m <sup>3</sup> /s)	Inflow (m <sup>3</sup> /d/m)
RM 166	March	200	-	-	-	-	-	-
	May	384	-	-	-	-	-	-
	August	384	-	-	-	-	-	-
	October	384	0.57	0.53	0.55	0.04	0.06	-0.84
	December	384	0.20	0.21	0.21	-0.01	0.02	0.06
RM 155	March	290	1.23	1.24	1.24	-0.01	0.12	0.06
	May	800	0.82	0.96	0.89	-0.13	0.09	1.44
	August	800	1.16	1.24	1.20	-0.08	0.12	0.91
	October	800	1.34	1.34	1.34	0.00	0.13	-0.03
	December	800	1.27	1.31	1.29	-0.04	0.13	0.42
RM 141	March	206	-	-	-	-	-	-
	May	206	0.14	0.17	0.15	-0.03	0.02	1.31
	August	206	0.06	0.08	0.07	-0.02	0.01	0.77
	October	206	0.01	0.01	0.01	0.00	0.00	0.00
	December	206	-	0.07	0.03	-	-	-
RM 135	March	188	0.42	-	0.42	-	0.02	-
	May	188	1.49	1.46	1.47	0.03	0.15	-1.31
	August	188	2.26	2.26	2.26	0.00	0.23	-0.05
	October	188	1.90	1.90	1.90	0.01	0.19	-0.26
	December	188	0.81	0.80	0.81	0.01	0.08	-0.35
RM 124	March	200	0.95	1.00	0.97	-0.05	0.10	2.30
	May	660	1.82	1.79	1.80	0.03	0.18	-0.43
	August	660	1.63	1.76	1.70	-0.13	0.17	1.73
	October	660	1.10	1.15	1.13	-0.05	0.11	0.59
	December	660	0.37	0.46	0.41	-0.09	0.04	1.18

Conventional gauging with a velocity meter and wading rod was performed at all sites, except where vegetation and/or flow conditions made it unreliable. Conventional gauge measurements can be expected to have a high degree of confidence due to the uniform geometry of the drains and high density of measurement intervals (0.3048 m/ 1 ft) across a given channel cross section. However, transient flow conditions (where discharge changes throughout the course of a measurement) or turbulence can introduce error. By convention, gauging by this method is considered to have a 5% margin of error, though in ideal conditions the actual error may be far lower. Conventional measurement records, errors, and calculated inflows are presented in Table 3.3. As with dilution gauging, where the difference between the downstream and upstream discharge measurements ( $\Delta Q$ ) is less than the error (where the error is the sum of each measurement times an assumed error of 5%) the inflow measurement are considered to be low confidence. Confidence in the calculated inflow increases with respect to the excess of the inflow relative to the error.

Drain discharge by conventional measurement ranged from 0.01 m<sup>3</sup>/s (0.4 CFS) at RM 141 during May to 2.26 m<sup>3</sup>/s (79.8 CFS) at RM 135 in August. Groundwater flux ranged from -13.1 m<sup>3</sup>/d/m (RM 135 in May) to 23.0 m<sup>3</sup>/d/m (RM 124 in March). For all sites, the average inflow was highest in March (13.3 m<sup>3</sup>/d/m) and lowest in October (-1.1 m<sup>3</sup>/d/m). Average inflow in May was 2.5 m<sup>3</sup>/d/m, 8.4 m<sup>3</sup>/d/m in August, and 3.7 m<sup>3</sup>/d/m in December. Average discharge across all sites was 1.0 m<sup>3</sup>/s (34.2 CFS) in March, 1.1 m<sup>3</sup>/s (38.1 CFS) in May, 1.3 m<sup>3</sup>/s (46.1 CFS) in August, 1.0 m<sup>3</sup>/s (34.8 CFS) in October, and 0.6 m<sup>3</sup>/s (21.6 CFS) in December. Except for May, RM 124 had the highest inflow rate of all sites. RM 135 had negative inflow rates for all available measurements and had the lowest inflow rate (or greatest loss rate) during all campaigns except October. RM 141 consistently had the lowest overall discharge (0.08 m<sup>3</sup>/s or 2.7 CFS), and RM 135 had the highest (1.48 m<sup>3</sup>/s or 52.2 CFS). Average discharge for the other sites was 0.38 m<sup>3</sup>/s (13.3 CFS) at RM 165, 1.19 m<sup>3</sup>/s (42.1 CFS) at RM 155, and 1.20 m<sup>3</sup>/s (42.5 CFS) at RM 124.

Several significant sources of error were present in the dilution gauging measurements. Mass loss of rhodamine in the channel due to sorption upon suspended sediment, vegetation, and bank materials was a pervasive issue evident by dramatically higher discharge values obtained by dilution gauging vs. manual gauging. Incomplete mass recovery of dye at measurement locations results in a smaller integrated value of the time/concentration curve, resulting in overestimations of flow. Disparity between conventional measurements and dilution measurements was greatest in May and August, when turbidity in the drains was high. Error also arose from variable background fluorescence, debris interference with the fluorometer optics, and the correction factors and integration limits used in the discharge calculations.

### **3.2 Water Chemistry**

Here, we present an overview and analysis of significant values and trends of isotopes, major ions, and trace metals. A complete record of field parameters, major and minor ions, trace metals, and isotopes analyzed for this study can be found in the electronic supplement. Major ions and strontium isotopes presented apparent spatial and seasonal trends. The field parameters provide useful context for geochemical controls and conditions (temperature, dissolved oxygen, pH, specific conductivity, total dissolved solids). Stable isotopic compositions of water ( $\delta^{18}\text{O}$  and  $\delta^2\text{H}$ ) showed trends in evaporation and water provenance. Mineral saturation indices provide context for mineralogical

controls on elemental availability and conservative ion behavior. Trace metal abundance informs redox conditions and water quality

### 3.2.1 Field Parameters

Field parameters including pH, specific conductance, dissolved oxygen (DO), and temperature were measured during or immediately before/after sample collection with the exception of the river sites in March and the river at RM 135 in May. The pH of all surface waters were neutral to somewhat basic, ranging from 7.52 to 8.67, averaging 8.1. Temperature varied significantly on diurnal and seasonal scales, averaging 17.6°C and ranging from 5.4°C to 33.4°C. Specific conductance ranged seasonally and spatially (Fig. 3.2), averaging 605  $\mu\text{S}/\text{cm}$ . DO values were high, averaging 97.9 %<sub>sat</sub> and 9.32 mg/L and ranging from 65.3 %<sub>sat</sub> and 6.84 mg/L to 165.8 %<sub>sat</sub> and 196.3 mg/L.

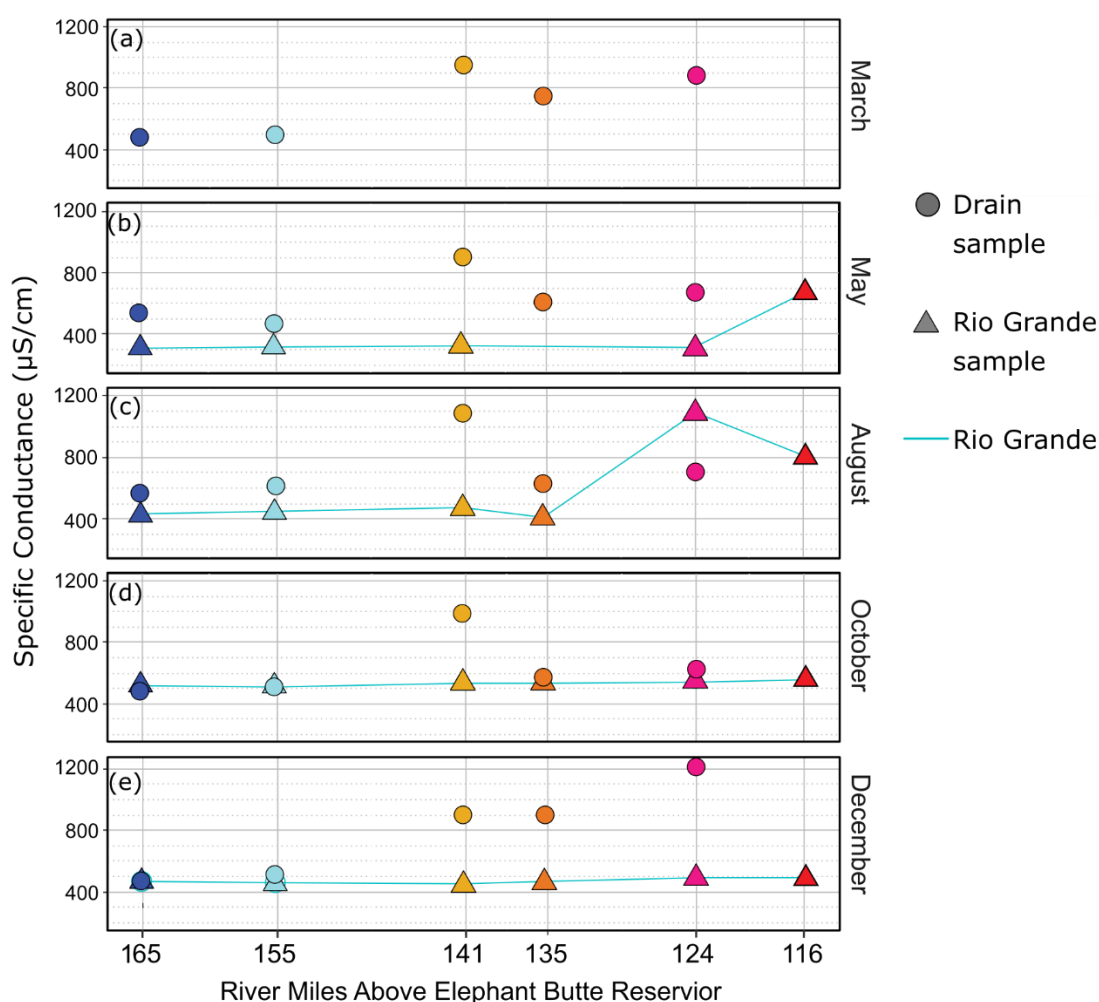


Figure 3.2. Specific conductivity trends along flow distance by campaign for rivers (triangles) and drains (circles). The blue line corresponds with the river. Measurements were not collected from the river in March. Measurements were collected in the field using a YSI EXO 1 Multiprobe.

### 3.2.2 Major Ions

Surface water samples throughout the project area were predominantly a calcium-bicarbonate water type, however some drain and river samples were a sodium-bicarbonate water type and occasionally a sodium-sulphate/chloride water type (Fig. 3.3). For all campaigns, we observed a general trend of increasing proportion of sodium relative to calcium, and increasing chloride and sulfate relative to bicarbonate from north to south. During the pre-irrigation sampling campaign in March (Fig. 3.3) all drain samples were a  $\text{Ca}^{2+}\text{-HCO}_3^-$  water type with the exception of RM 124 which was a  $\text{Na}^+\text{-HCO}_3^-$  type (Fig. 3.3). Although most of the drains were a  $\text{Ca}^{2+}\text{-HCO}_3^-$  type, the proportion of  $\text{Ca}^{2+}$  to  $\text{Na}^+$  (in meq %) decreased from 10% to about 3% following a near linear trend against to flow distance, before reaching RM 124, where  $\text{Na}^+$  became dominant over  $\text{Ca}^{2+}$  by about 5 meq%. Only two river samples were collected in March, from RM 116 and San Acacia (RM 116). Similar to the trend seen in the drains, the RM 165 river sample was a  $\text{Ca}^+\text{-HCO}_3^-$  water type and the RM 116 river sample was a  $\text{Na}^+/\text{Ca}^{2+}\text{-HCO}_3^-$ , where  $\text{Na}^+$  and  $\text{Ca}^{2+}$  were in near-even proportion with  $\text{Na}^{2+}$  slightly dominate.

We also observed increases of  $\text{Cl}^-$  with proximity to the basin's terminus in March (Fig. 3.4). This trend was most pronounced in the river, where  $\text{Cl}^-$  concentration at RM 165 (Bosque Farms) was 21.2 ppm and 50.5 ppm at RM 116 (San Acacia). This amounts to an increase of 138%. The drain network in March also had generally higher  $\text{Cl}^-$  concentrations to the south. This was a near-linear trend from 25.1 ppm at RM 165 to 61.6 ppm at RM 124, however the linear trend was disrupted by a spike at RM 141 to 57.8 ppm before returning to 38.6 at RM 135. The chloride mass flux (Fig. 3.5) also generally increased with flow distance; however the trend is less apparent in the drains due to the variable discharge. In the river,  $\text{Cl}^-$  flux increased from approximately 300 to 700 kg/day between RM 165 and RM 116.

The May sampling campaign was performed during spring runoff. This was the only campaign in which all samples were a  $\text{Ca}^+\text{-HCO}_3^-$  water type (Fig. 3.3) The trend of increasing proportions of  $\text{Na}^+$  to  $\text{Ca}^{2+}$  and  $\text{Cl}^- + \text{SO}_4^-$  to  $\text{HCO}_3^-$  was still apparent in the drains, but this trend was not pronounced in the river.  $\text{Cl}^-$  concentration (Fig. 3.4) and mass flux (Fig. 3.5) are similar in trend and magnitude in the drains as compared to March but are significantly different in regard to the river. During this campaign (and throughout future campaigns) samples from the river were collected adjacent to each site. River  $\text{Cl}^-$  concentration varied between 10.6 and 11.6 ppm between RM 165 and RM 124, increasing to 13.8 ppm at RM 116 (Fig. 3.4).  $\text{Cl}^-$  mass flux varied between 2000 kg/day and 3000 kg/day, increasing overall across the project area with local variations (Fig. 3.5).

August samples had a greater range in meq% difference in  $\text{Ca}^{2+}$  vs.  $\text{Na}^+$  than March but a similar range in  $\text{HCO}_3^-$  relative to  $\text{Cl}^- + \text{SO}_4^-$  (Fig. 3.3). In the drains, the trend was similar to March with the exception of a higher proportion of  $\text{Ca}^{2+}$  to  $\text{Na}^+$  at RM 165. The river had the broadest distribution of any campaign with respect to both anions and cations. The river samples from RM 165 to RM 141 were all  $\text{Ca}^{2+}\text{-HCO}_3^-$  type and followed the regional trend. RM 124 shifted ~10 meq% relative to RM 135 with respect to dominant cations without a significant change in dominant anions, becoming a  $\text{Na}^+\text{-HCO}_3^-$  type water. At RM 116, the river shifted almost 20 meq% towards  $\text{Na}^+$  dominance and ~5 meq% towards  $\text{Cl}^-/\text{SO}_4^-$  dominance, becoming a sodium-sulphate type water. River chloride concentrations were variable in August. River concentration increased overall from 23.1 to

33.8 ppm over the project area, however a low of 18.8 ppm was measured at RM 141 (Fig. 3.4). This anomaly at RM 135 was not apparent in the mass flux (Fig. 3.5), which remained steady at approximately 500 kg/day from RM 165 to RM 141 and subsequently increased to over 1000 kg/day between RM 135 and RM 116.

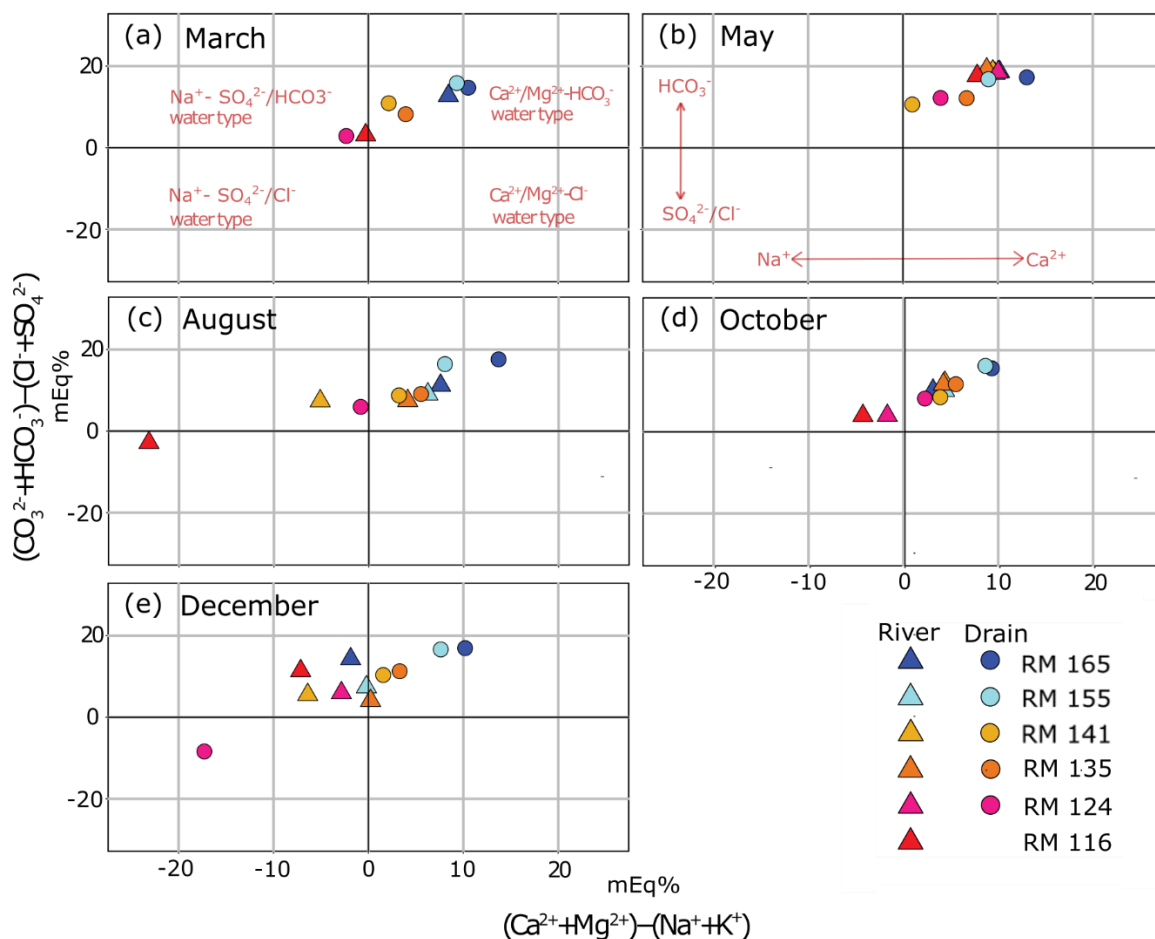


Figure 3.3. Boxplot of major ion proportions and major water types of samples during each campaign. Symbols correspond to Figure 3.1. Circles indicate drain samples and triangles indicate river samples. The color scale goes from blue (north) to red (south).

In October all drains were once again a  $\text{Ca}^{2+}\text{-HCO}_3^-$  type (Fig. 3.3). RM 165 and RM 155 had very similar major ion proportions, as did RM 135 and RM 124 – although RM 124 was slightly less  $\text{Ca}^{2+}$  dominant (Fig. 3.3). The river at sites RM 165 through RM 135 were all very similar as well and were a  $\text{Ca}^{2+}\text{-HCO}_3^-$  type (Fig. 3.3). The major ion chemistry river at RM 124 and RM 116 departed from the others considerably, plotting as a  $\text{Na}^+\text{-HCO}_3^-$  type (Fig. 3.3). RM 116 had a 2-3 meq% increase in  $\text{Na}^+$  dominance from RM 124 but remained stable with respect to anion proportions (Fig. 3.3). Chloride concentrations decreased overall from 37.3 ppm at RM 165 to 35.9 ppm at RM 116, ranging variably to a low of 33.7 ppm at RM 124 (Fig. 3.4). The river chloride mass flux

was roughly uniform stable throughout the project area at just shy of 2000 kg/day, dropping slightly at RM 141 (Fig. 3.5).

In December, drain sites RM 165 through RM 135 were  $\text{Ca}^{2+}\text{-HCO}_3^-$  type and had a trend of decreasing  $\text{Ca}^{2+}$  and  $\text{HCO}_3^-$  with downstream distance (Fig. 3.3). The RM 124 drain followed the general trend set by drain sites RM 165 through RM 135, but became  $\text{Na}^+\text{-SO}_4^-$  dominant (Fig. 3.3). That same sample also had the highest chloride concentration observed in the study of 131.0 ppm (Fig. 3.4). The river samples from December were all  $\text{Na}^+/\text{Ca}^{2+}\text{-HCO}_3^-$  or  $\text{Na}^+\text{-HCO}_3^-$  type water and did not have a discernible trend (Fig. 3.3) Chloride concentration (Fig. 3.4) and mass flux (Fig. 3.5) in the river increased overall throughout the project area, but in fact decreased between RM 165 and RM 141. River samples from December were dominantly sodic and highly variable.

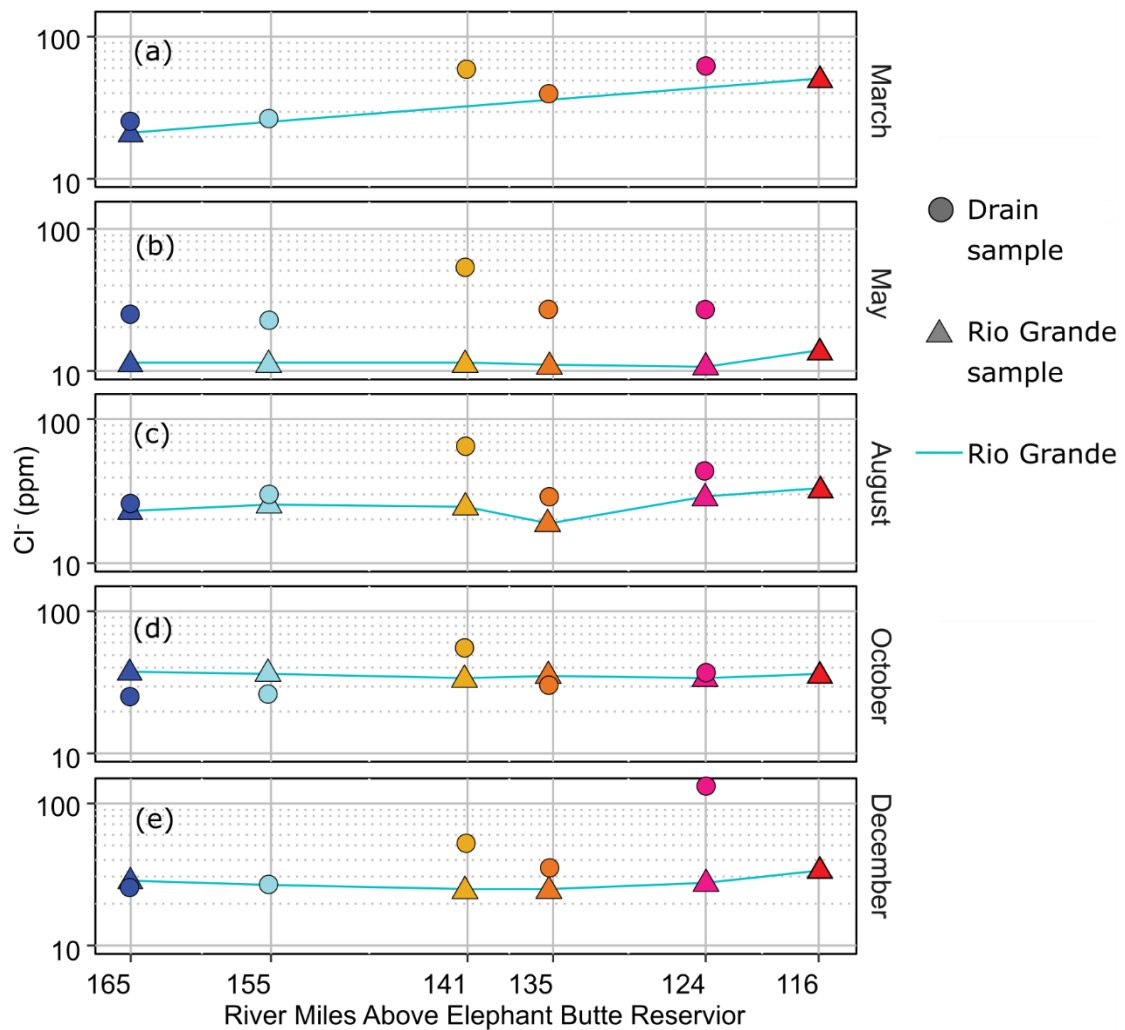


Figure 3.4.  $\text{Cl}^-$  concentration (ppm) along flow distance in drains (circles) and the Rio Grande (triangle) during individual measurement campaigns. The blue line corresponds with the river.

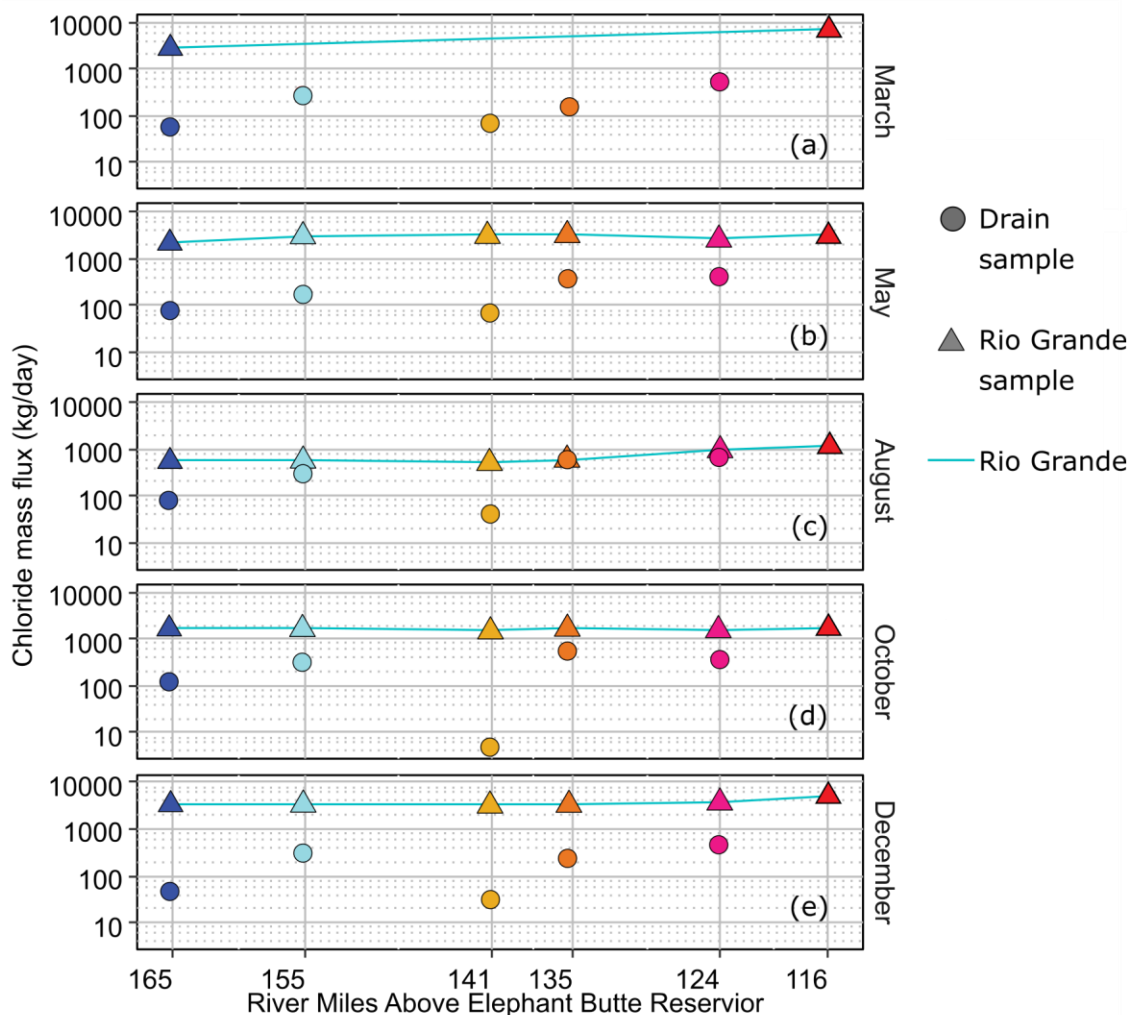


Figure 3.5. Trends in Cl<sup>-</sup> mass flux (kg/day) along flow distance in drains (circles) and the Rio Grande (triangle) during individual measurement campaigns. The blue line corresponds with the river.

### 3.2.3 Trace Metals

The abundance for individual trace metals followed a similar trend for all samples, but variability of certain individual elements could vary across a range exceeding one order of magnitude (Fig. 3.6). No samples exceeded the maximum contaminant limit (MCL) for any of the elements measured except for the RM 165 drain in December, which exceeded the MCL of 10 ppb for arsenic by 3.3 ppb. Many of the elemental distributions were limited by the lower reporting limit for the analysis method, which varies by element. Iron for instance has a reporting limit of 0.01 mg/l (ppm), resulting in a bimodal distribution of samples that is difficult to interpret (Fig. 3.6). An even more pronounced bimodal distribution is apparent with titanium, whose lower reporting limit of titanium is 0.001 mg/l.



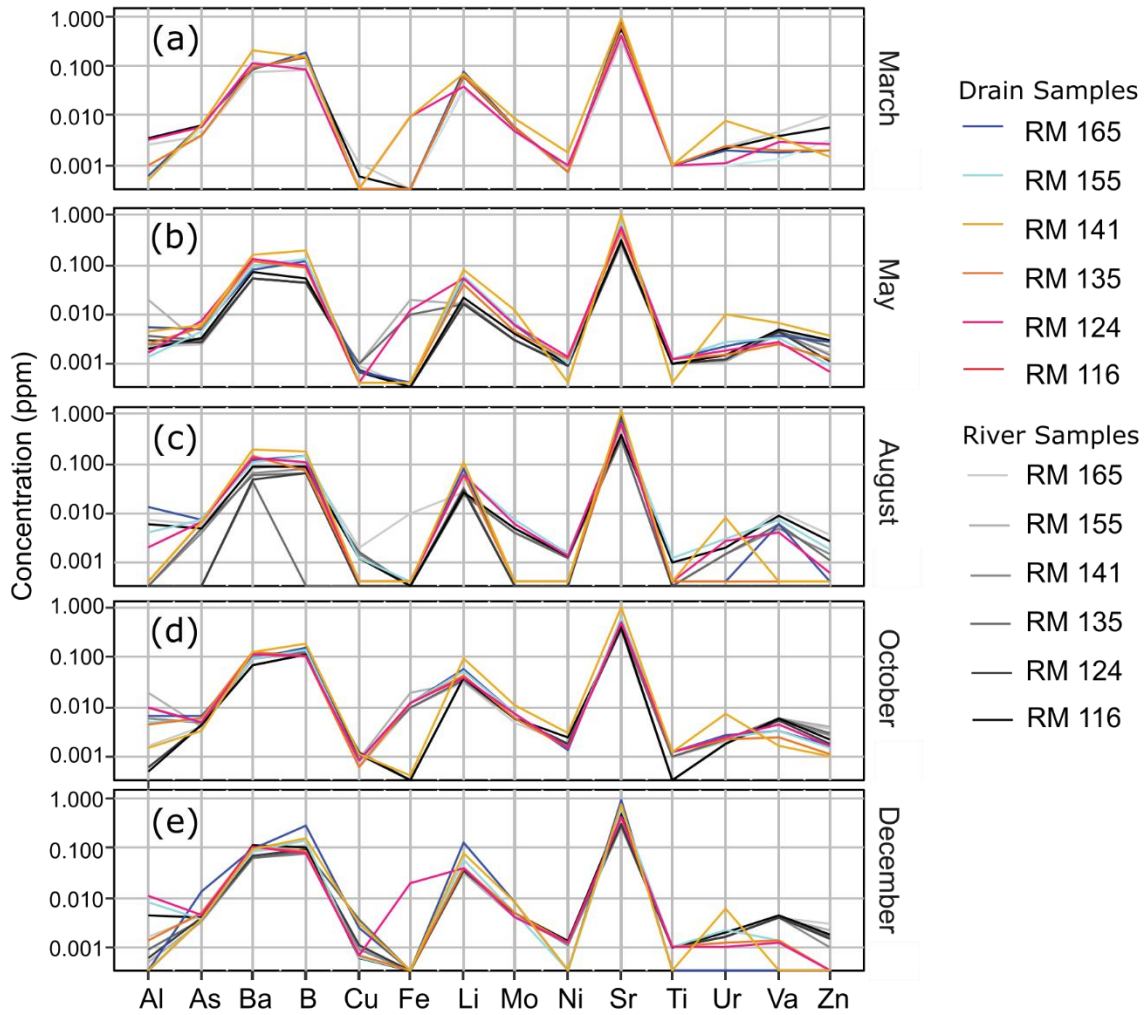


Figure 3.6. Spiderplots of trace metal concentration (ppm) of all samples by month.

The RM 141 drain consistently had the highest overall trace metal concentration across all campaigns (Fig. 3.6). Uranium was particularly elevated at this site relative to the other sites. Uranium is relatively common in granitic rocks and can be soluble in reduced (tetravalent) or oxidized (hexavalent) forms, although the solubility of reduced uranium is limited (Clark, 2015). With the exception of the December campaign, the RM 141 drain also had the highest strontium concentration, which has implications relevant to mixing calculations discussed in Section 4.3. Many elements had highly variable concentrations that were inconsistent across locations and campaigns. Aluminum is perhaps the most noticeably variable example (Fig. 3.6). Aluminum as well as iron are common weathering products of felsic and mafic minerals, respectively. Lithium was a common constituent in both drain and surface waters up to about 0.1 ppm.  $\text{Li}^+$  is highly soluble and behaves conservatively, can be introduced to groundwater systems from both weathered granitic bedrock and evaporite deposits (Clark, 2015).

### 3.2.4 Stable Isotopes

Stable isotopes of water include  $\delta^{18}\text{O}$  and  $\delta^2\text{H}$  are presented by campaign in Figure 3.7. Seasonal and spatial trends are subtle but apparent. Samples typically plotted near the local meteoric water line (LMWL) from Plummer et al. (2004) and trended along slopes of 4.0 to 8.0 (Fig. 3.7).

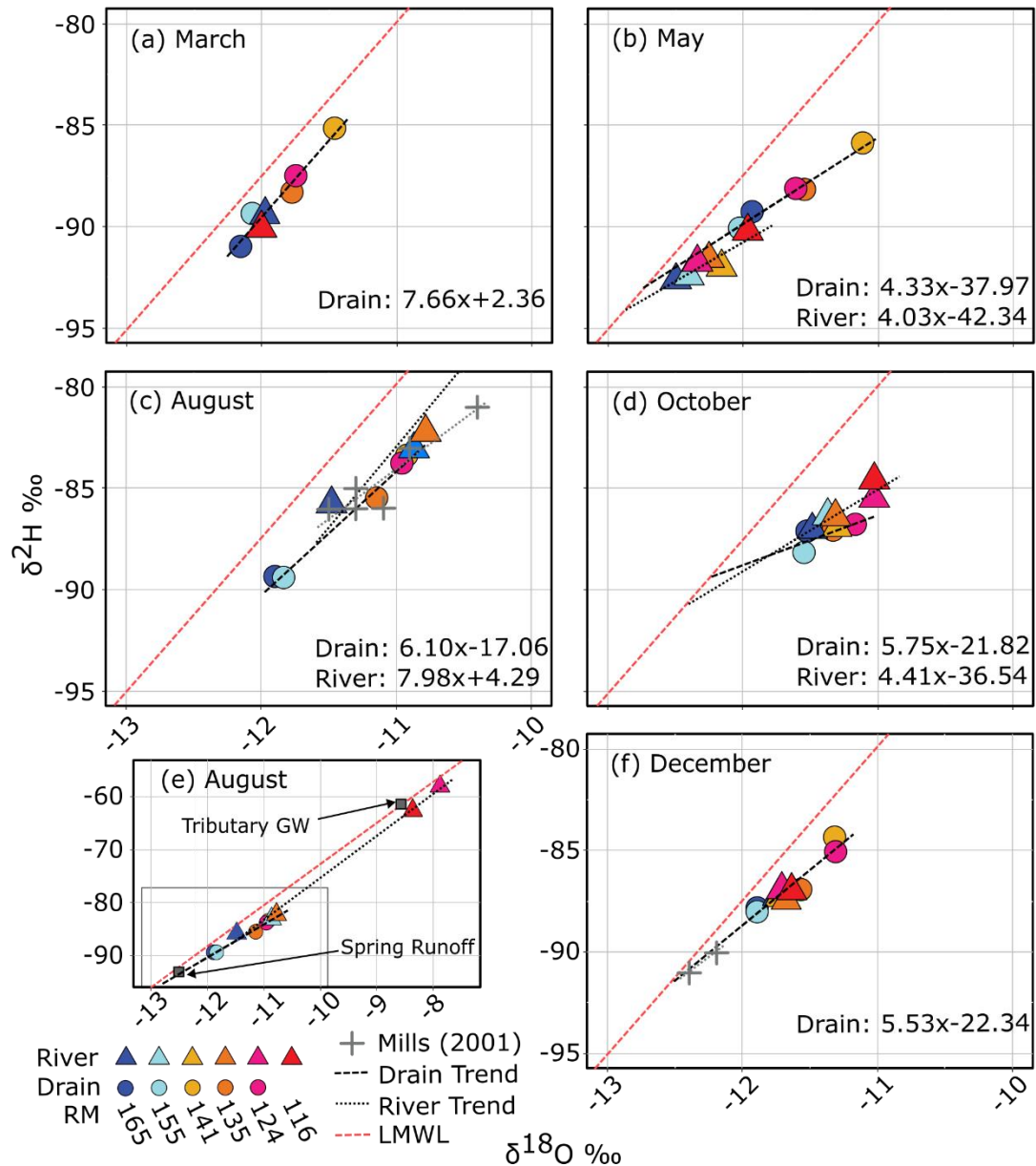


Figure 3.7. Monthly trends in  $\delta^{18}\text{O}$  vs.  $\delta^2\text{H}$  of drain (circle) and river (triangle) samples colored by river mile (upstream/north beginning with dark blue grading to red downstream/south). The local meteoric water line (LMWL) follows the form:  $\delta^2\text{H} = (7.73) \delta^{18}\text{O} + 4.73$  (Plummer et al., 2004). Data from Mills (2001) collected in the project area during January and August of 2001 is shown on plots (f) and (c) respectively.

The degree of evaporation in water samples was calculated the using a  $\delta^{18}\text{O}$  Rayleigh distillation model for river and drain samples that trended along slopes of less than 7 during a given campaign (Fig. 3.7; Table 3.4; Table 3.5). Evaporation causes the  $\delta^{18}\text{O}$  vs.  $\delta^2\text{H}$  slope to vary between about 4 and 7 depending on relative humidity (RH), a slope of 6 corresponds to a RH of ~ 80%, a slope of 5 corresponds to a RH of ~50%, and a slope of 4.2 corresponds to a RH of ~20%; the suggested RH indicates the appropriate evaporative enrichment factor for calculating the evaporated fraction (Clark, 2015). Sample data that trended along a slope greater than 7 were assumed to not have an evaporated signature. The RM 165 river and drain samples were used as the initial composition for the subsequent evaporation in the river and drains for a given month. This analysis does not account for the effect of mixing.

Month	Slope	RH	RM 155	RM 141	RM 134	RM 124
May	4.3	20%	-0.5%	4.2%	2.0%	1.7%
August	6.1	80%	0.5%	7.3%	5.7%	7.0%
October	5.8	80%	-0.2%	10%	1.5%	2.8%
December	5.5	50%	0.0%	3.4%	1.9%	3.5%

Table 3.4. Drain water evaporation calculated following Clark (2015). The RM 165 drain composition was used as the source water.

Month	Slope	RH	RM 155	RM 141	RM 134	RM 124	RM 116
May	4	20%	0.5%	1.8%	1.3%	0.8%	2.7%
October	4.4	20%	0.6%	0.9%	0.9%	2.4%	2.3%

Table 3.5. River water evaporation for May and October calculated following Clark (2015). The RM 165 river composition was used as the source water.

### 3.2.5 Strontium Isotopes

Samples were collected and analyzed for the ratio of strontium-87 to strontium-86 for drain sites and the river adjacent to Bosque Farms (RM 165) and at San Acacia, (RM 116). The  $^{87}\text{Sr}/^{86}\text{Sr}$  ratio value and trends were variable during each campaign, particularly in the river (Fig. 3.8).

During the March campaign  $^{87}\text{Sr}/^{86}\text{Sr}$  in the river increased from  $0.70955 \pm 0.00016$  to  $0.70996 \pm 0.00003$  (Fig. 3.8). RM 165 and RM 155 drains both had a value of  $0.70999$ , with errors of  $0.00003$  and  $0.00002$  respectively. RM 141 had the highest value observed in the campaign of  $0.71013 \pm 0.00002$ . A downward trend in  $^{87}\text{Sr}/^{86}\text{Sr}$  was observed in the RM 135 and RM 124 drains, which had values of  $0.70987 \pm 0.00003$  and  $0.70966 \pm 0.00003$  respectively. This downward trend was persistent throughout all campaigns, with RM 124 consistently having the lowest  $^{87}\text{Sr}/^{86}\text{Sr}$  ratio of all the drains analyzed.

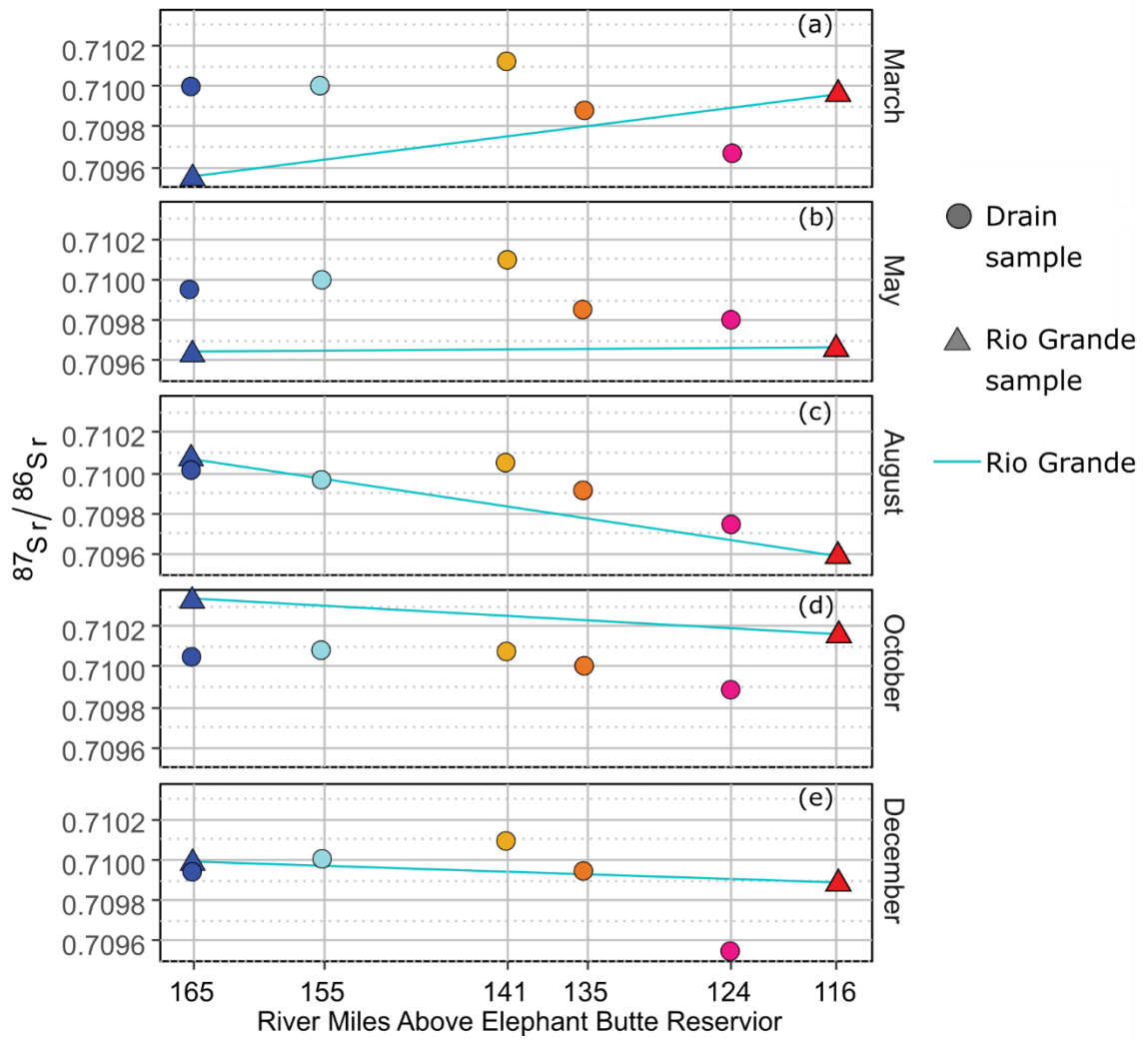


Figure 3.8. Strontium isotope trends along flow distance by campaign for the river (triangles) and drains (circles). The blue line corresponds with the river. (Clark, 2015)3

$^{87}\text{Sr}/^{86}\text{Sr}$  varied minimally in the river during May (Fig. 3.8), increasing slightly from  $0.70965 \pm 0.00008$  to  $0.70967 \pm 0.00011$ , an increase in the ratio of only 0.00001 units away from being within error window. The overall  $^{87}\text{Sr}/^{86}\text{Sr}$  trend in the drains remained consistent with March, particularly between RM 165 and RM 141 that changed below measurement precision between March and May. The RM 135 drain was slightly lower than March ( $^{87}\text{Sr}/^{86}\text{Sr} = 0.70984 \pm 0.00004$ ) and the RM 124 drain was slightly higher ( $^{87}\text{Sr}/^{86}\text{Sr} = 0.70980 \pm 0.00002$ ). Discharge in those two sites were higher in May than in March.

In August the  $^{87}\text{Sr}/^{86}\text{Sr}$  trend in the river reversed relative to March, decreasing from  $0.71007 \pm 0.00003$  at RM 165 to  $0.70959 \pm 0.00001$  at RM 116 (Fig. 3.8). The drains remained fairly similar to previous months. The RM 165 drain increased to its highest value so far to  $0.71002 \pm 0.00002$ , while the RM 155 and RM 141 drains decreased to their lowest value yet at  $0.70997 \pm 0.00002$  and  $0.71005 \pm 0.00001$  respectively. The RM 135 drain

reached its highest value yet at  $0.70991 \pm 0.00002$ , and the RM 124 drain reached a median value of  $0.70975 \pm 0.00003$ .

The overall decrease of  $^{87}\text{Sr}/^{86}\text{Sr}$  in the river continued in October (Fig. 3.8) but had the highest overall values observed in the study ( $0.71034 \pm 0.00002$  at RM 165 and  $0.71016 \pm 0.00005$  at RM 115). The RM 165 and RM 155 drains also reached their highest values of the study ( $0.71005 \pm 0.00003$  at RM 165 and  $0.71008 \pm 0.00011$  at RM 155). The RM 141 drain was consistent with previous campaigns at  $0.71007 \pm 0.00003$ . RM 135 and RM 124 also had their highest points of the study at  $0.71000 \pm 0.00003$  and  $0.70988 \pm 0.00002$  respectively.

The river at RM 165 had an  $^{87}\text{Sr}/^{86}\text{Sr}$  value of  $0.70993 \pm 0.00002$  in December (Fig. 3.8), lower than August and October but still above the March and May values. The RM 116 river sample had a value of  $0.70989 \pm 0.00003$ , just  $0.00007 \pm 0.00006$  from its value in March. The trend in the drains between RM 165 and RM 141 resembled the trend in March and May, increasing linearly from  $0.70994 \pm 0.00002$  at RM 165 to  $0.71009 \pm 0.00005$  at RM 141. The RM 135 drain decreased from the October value to  $0.70995 \pm 0.00004$ , which was still higher than other months. The RM 124 drain reached an all-time low value of  $0.70954 \pm 0.00003$ .

### 3.2.6 Mineral Saturation Indices

Saturation indices (SI) were calculated from surface water sample data collected throughout the project using the Geochemist's Workbench Community Edition (version 15.0) software suite (Fig. 3.9). However, the program was not able to calculate SI values for several samples. The reason for this is unclear and may be due to significant disequilibrium conditions present in the system at the time of sample collection, however charge imbalances from water sample analysis were  $<|5|\%$  except for the river in December at RMs 165, 155, and 116 which were each  $\sim|6|\%$  imbalanced (see electronic supplement). Of the minerals evaluated, anorthite (Ca-feldspar) was the most undersaturated, which has implications for Sr concentrations and  $^{87}\text{Sr}/^{86}\text{Sr}$  ratios (see Section 4.3). Calcite, dolomite, and quartz were all saturated or supersaturated. Clay minerals (illite, kaolinite) were both near equilibrium, with outlier values of  $\text{SI} \approx -3$ .

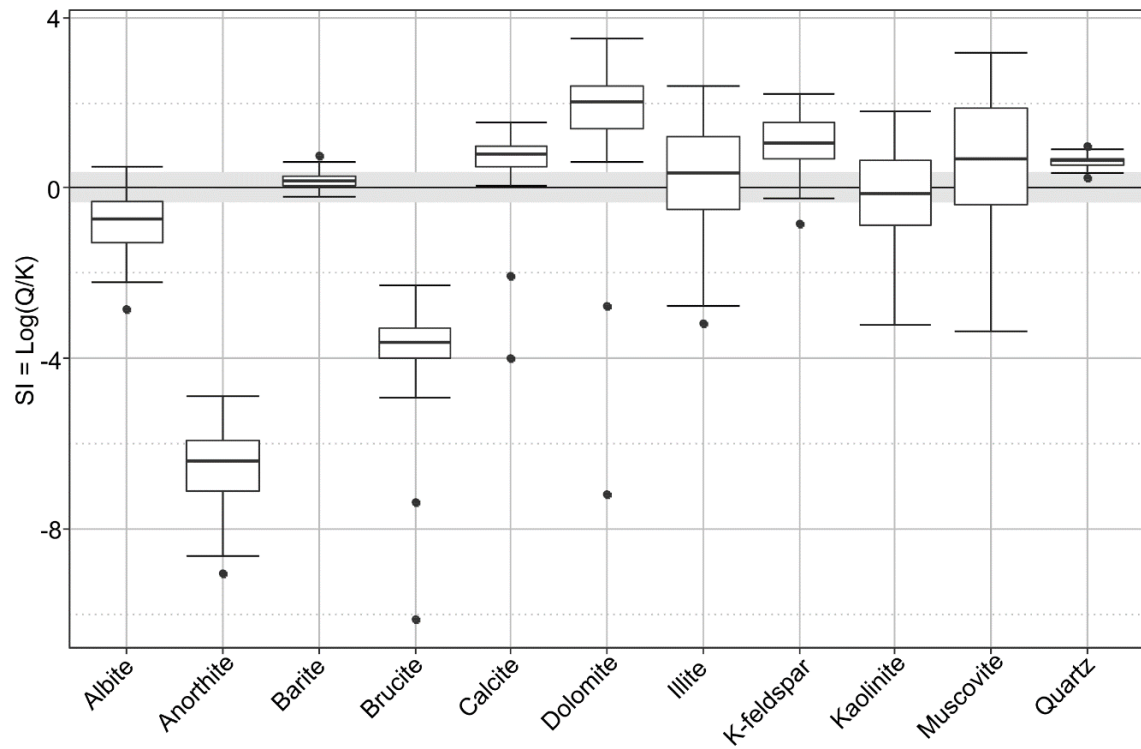


Figure 3.9. Saturation indices (SI) of select minerals calculated from surface waters. The grey region covers the near equilibrium region of  $SI = \pm 0.5$ .

## CHAPTER 4

### DISCUSSION

#### 4.1 Discharge Trends

Total discharge and the rates of groundwater inflow provide the volumetric component of the mixing system. Of the three methods for determining groundwater inflow, radon gauging is the most informative of the overall system because (1) it integrates a greater area compared to the differential gauging approaches used, (2) it is less sensitive to compounding errors in gauge measurements, (3) it was consistently applied throughout the study without issue (with the exception of equipment failure in August). Of these points, (1) is the most significant to our purposes. Radon is inherited over a fairly long flow distance (although the length is limited by degassing) in the same manner that solute is accumulates (Cook, 2013). The physical methods of flow gauging used were applied over an interval of less than a kilometer – wherein the chemistry of the waters may not significantly change. Thus, the inflow rate determined by physical gauging may not be relevant to the conditions that contribute to the chemistry of the waters that were samples. Inflow determined from radon and the other methods is given in Table 4.1. Values determined from the radon method ranged from 0.38 to 6.61 m<sup>3</sup>/d/m. Inflow rates were highly variable throughout time and space, which could be explained by a myriad of local and seasonal perturbations.

Average discharge in the drains (Table 3.3) was highest in August (13.1 m<sup>3</sup>/s), followed by October (9.9 m<sup>3</sup>/s), May (9.4 m<sup>3</sup>/s), March (8.8 m<sup>3</sup>/s), and December (5.6 m<sup>3</sup>/s). Average inflow from radon was highest in March (5.1 m<sup>3</sup>/d/m), followed by May (3.9 m<sup>3</sup>/d/m), October (2.1 m<sup>3</sup>/d/m), December (1.7 m<sup>3</sup>/d/m), and August (0.5 m<sup>3</sup>/d/m). The average radon inflow value from august only consists of the RM 135 and RM 124 sites, so it is not an accurate representation of the entire project area. Peak drain discharge during August is consistent with peak irrigation and a runoff component in drain flow. The fact that drain discharge is higher during irrigation season demonstrates that irrigation return flows are a significant driver of drain flow. No clear relationship between discharge and inflow presented itself. Total discharge is indicative of regional conditions, while inflow rates are dependent on more local conditions – so the lack of a clear relationship between the two parameters simply reinforces that the datasets should be independently interpreted. The magnitude of discharge at individual drains generally scaled with respect to the amount of upstream drain network (Table 3.2).

The RM 165 and RM 155 drains had high average inflow rates determined from radon (3.7 and 5.0 m<sup>3</sup>/d/m respectively). The RM 155 drain is adjacent to a section of the Rio Grande that is prone to drying (McKenna, 2019) and both drains are completed deeper than the bed elevation of the Rio Grande (Section 2.1). This suggests that seepage from the Rio Grande accounts for a high proportion of inflow to these drains, particularly RM 155. The RM 141 drain had a moderate inflow rate despite having a low overall discharge (Table 3.3; Table 4.1). The Rio Grande is not prone to drying in the RM 141 vicinity (McKenna, 2019) suggesting that inflow in this region is driven by regional groundwater. The RM 135 drain had a moderate inflow rate determined by radon (Table 4.1) but conventional differential measurements showed that it consistently had a negative flux rate. This can be explained by the presence of a dam structure just below the differential measurement below which the water level in the channel was 2-3 m lower. Loss in this section was likely driven by this local negative gradient. The Rio Grande is prone to drying near this site (McKenna, 2019), which suggests that seepage from the Rio Grande is entering the drain in this area which would explain the moderate inflow rate indicated by the radon measurements.



Drain Site	Month	[ <sup>222</sup> Rn] (Bq/L)	Radon Inflow (m <sup>3</sup> /d/m)	Conventional Inflow (m <sup>3</sup> /d/m)	Dilution Inflow (m <sup>3</sup> /d/m)
RM 165	March	53.3 ± 1.2	5.70	-	-0.10
	May	60.2 ± 1.7	6.61	-	0.64
	August	-	-	-	-
	October	6.4 ± 2.6	0.73	-0.84	0.01
	December	17.6 ± 4.2	1.93	0.06	0.48
RM 155	March	38.7 ± 1.3	5.94	0.06	-3.13
	May	36.3 ± 1.3	6.34	1.44	-3.03
	August	-	-	0.91	0.71
	October	31.5 ± 8.6	5.35	-0.03	0.92
	December	12.2 ± 3.5	2.35	0.42	0.83
RM 141	March	27.7 ± 0.8	2.36	-	3.61
	May	34.0 ± 1.2	3.74	1.31	1.14
	August	-	-	0.77	-2.13
	October	2.7 ± 2.4	0.57	-	-
	December	5.0 ± 2.2	0.47	2.81	0.21
RM 135	March	42.8 ± 1.5	6.23	-19.34	9.86
	May	16.7 ± 0.9	2.45	-1.31	-5.02
	August	4.1 ± 0.7	0.62	-0.05	4.52
	October	20.2 ± 4.6	3.19	-0.26	3.41
	December	11.2 ± 3.5	2.45	-0.35	1.07
RM 124	March	-	-	2.30	-0.12
	May	5.6 ± 0.3	0.55	-0.43	-1.43
	August	3.8 ± 0.3	0.38	1.73	1.69
	October	8.9 ± 4.3	0.82	0.59	0.86
	December	9.2 ± 3.0	1.29	1.18	0.18

Table 4.1. Radon activity and inflow rate overview.

The RM 124 drain had a low inflow as determined by radon, but a high inflow rate determined by conventional gauging (Table 4.1). The radon inflow rate at this site is probably erroneous (discussed below) and the high average inflow rate determined by conventional gauging is consistent with its proximity to the distal basin and regional water table gradients (Fig. 1.4). Potential error in the radon method arise from sampling error (as Rn can easily de-gas) and choice of empirical coefficient values used for the calculations (Cook, 2013). Unfortunately, we could not take site-specific gas transfer velocity measurements. Inflow at the RM 124 site was probably underestimated due to an underestimation of the gas transfer velocity – which can be assumed to be higher than at other locations due to numerous dam structures. The variability in the activity of radon in riparian groundwater may also lead to misestimates.

Conventional flow gauging provided the most accurate measurement of total discharge at a given site. In most cases, the difference in discharge between the upstream and downstream measurements taken for differential gauging were within error of each other, limiting their utility for determining groundwater inflow rates (Table 3.3). Unlike the other methods used, differential flow gauging with conventional methods can accurately measure loss in flow, which was observed in many instances. Loss was consistently recorded across the measurement interval in the RM 135 drain (although never outside of error). This makes sense given the presence of a hydraulic jump immediately downstream of the measurement window. The dilution method was intermittently successful and could well with the conventional measurements – however in the presence of high turbidity this method generally failed to perform (Table 3.2).

## 4.2 Trends in Geochemistry and Water Isotopes

During all campaigns, drain water demonstrated an increase in sodium relative to calcium, and chloride and sulphate relative to bicarbonate with proximity to the basin's outlet. This trend was also observed in the river, except for May and October where minimal changes in major ions were observed (Fig. 3.3). Trends in cation concentration are interpreted to reflect cation exchange and mineral precipitation/dissolution in addition to mixing with sodic groundwater. It is difficult to resolve the relative effect of mixing, cation exchange, and mineral precipitation/dissolution on the trend due to the non-conservative behavior of the cations considered.

The increase in chloride and sulphate towards the terminus of the basin followed a similar trend as TDS, which is consistent with the prevailing theory that Middle Rio Grande salinization is driven by geologic solute inputs (Hogan et al., 2007; Phillips et al., 2003). However, one study using argued that sulphate additions in the middle and lower Rio Grande were derived from fertilizer but chloride additions were from a geologic source on the basis of  $\delta^{34}\text{S}$  data (Szynkiewicz et al., 2015). While it is possible that fertilizer contributes some sulphate to the system, our data does not indicate that fertilizer is a primary source of sulphate within our project area. The highest concentration of sulphate observed in this study was in the river in August at RM 124 (351 mg/L) immediately below the Rio Puerco confluence, which was flowing into the Rio Grande at the time of sampling. The sulphate concentration above the confluence at RM 135 was just 56.4 mg/L. The Rio Puerco watershed is devoid of significant agriculture or fertilizer use but has abundant exposed sulphate-rich evaporite deposits. This observation unambiguously demonstrates geologic sulphate's capacity to significantly impact the system. Additionally, drain sulphate concentrations were typically higher during the winter months when irrigation return flows were absent, particularly below RM 141. Moreover, fertilizer use is not known to be extensive in this region. The range of fertilizer  $\delta^{34}\text{S}$  used in the study mentioned overlaps with typical values of  $\delta^{34}\text{S}$  in igneous rocks and sedimentary pyrite (Clark, 2015) Sulphate derived from marine shale or igneous rock/sediment would be difficult to distinguish from fertilizer – and both alternative geologic sources of sulphate are present in the system.

Above the Rio Puerco confluence, a conservative estimate of the relative abundance of valley alluvium constituents may be 14% illite, 10% smectite, 1% SOM and 75% quartz,

based on previous discussion (Section 1.2.2). Using average cation exchange coefficient (CEC) values of 25 cmolc/kg for illite, 90 cmolc/kg for smectite, and 300 cmolc/kg for SOM, the average bulk soil CEC is 62 cmolc/kg (Eash, 2016). CEC south of the Rio Puerco is harder to estimate but is likely higher due to a higher overall clay fractions sourced from clay rich Paleozoic-Mesozoic sediments in the Abo and Puerco watersheds. Calcium has a greater force of attraction to exchange surfaces than sodium, therefore water interacting with valley sediment can be expected to preferentially exchange calcium for sodium. The increase in  $\text{Ca}^{2+}/\text{Na}^+$  in phreatic waters can therefore be explained by this exchange process alone, owing to the fact that waters farther along the flow path have presumably had longer residence times.

The  $\text{Ca}^{2+}/\text{Na}^+$  ratio may also be influenced by mineral precipitation or dynamic equilibration with Rio Puerco sediments. Loss of calcium from solution into the mineral phase is predicted by positive saturation indices (0 to 0.9) for calcite as well as high residual sodium carbonate parameters ( $>2.5$ ), which together indicate favorable conditions for the loss of calcium by precipitation (Essington, 2004). This possibility is favored by the presence of non-pedogenic calcium carbonate (vadose and phreatic cements) in outcrops of the Sierra Ladrone formation (Hall et al., 2004).

The trends of increases in salinity and sodicity with downstream distance were similar for valley soils and sampled waters (Fig. 1.3; Fig. 3.3; Fig. 3.4), and a shift towards increased salinity and salinity in the vicinity of Abo Arroyo and the Rio Puerco is evident. Surface and groundwater associated with the Rio Puerco and Abo Arroyo is highly sodic and has a high ionic strength (Plummer et al., 2004), promoting the precipitation of sodium salts and the occupation of exchange sites by sodium – which may in fact cause the shift in soil SARs and surface salinity (Fig. 1.3).

Temporal and spatial trends are further elucidated by the stable isotopes of water (Fig. 3.7). Variations in  $\delta^{18}\text{O}$  and  $\delta^2\text{H}$  across time and space inform the degree of mixing, source evolution, and evaporation throughout the project area. Unfortunately, the  $\delta^{18}\text{O}$  and  $\delta^2\text{H}$  values of various endmember waters are either unknown or do not vary significantly enough to use for rigorous mixing analysis. Winter precipitation (runoff from snowmelt) is isotopically lighter than summer precipitation (monsoon rains; Phillips et al., 2003). The data collected demonstrates the relative abundance of these distinct sources (Fig. 3.7). A simple  $\delta^{18}\text{O}$  mixing model was performed comparing the proportion of snowmelt runoff water ( $\delta^{18}\text{O} = -12.4\text{‰}$ ) and monsoon precipitation ( $\delta^{18}\text{O} = -63.4\text{‰}$ ) was performed, which showed that drain waters ranged between 71-91% snowmelt runoff water in March, 57-85% snowmelt runoff water in August, and 68-83% snowmelt runoff water in December. Lower fractions of snowmelt runoff water were encountered in the southern half of the project area.

During baseflow conditions in March, drain samples plot close to the local meteoric water line (LMWL), becoming more enriched along flow distance with the exception of the RM 141 drain – which was more enriched than the other sites (Fig. 3.7a). This trend was reversed in the river. This could be due to mixing, which can be expected due to the increase in discharge and solute load recorded throughout the project area during this window. However, the river samples were collected several days apart so this trend may be due to transient flow. The proximity of the drain sites to the LMWL and the absence of an evaporative trend suggests that evaporated waters (such as irrigation return flows) were

not present in the system, and the waters present were characteristic of baseflow that was not well connected to the land surface.

Drain samples were more enriched in  $\delta^{18}\text{O}$  overall in May (Fig. 3.7b) and demonstrated an evaporative trend (slope of 4.3). Irrigation began on April 1<sup>st</sup>, so this trend in the drains suggests that evaporated irrigated return flows had entered the system. River samples had an evaporated trend as well (slope of 4). However, a Rayleigh distillation model (Table 3.4) indicated that evaporation only ranged from 0.5-2.7% in the river, consistent with chloride concentrations and conductivity remaining relatively constant.

The river and the drains alike were highly enriched in August relative to the rest of the year with the exception of the RM 165 and RM 155 drain sites, which remained near their baseflow value (Fig. 3.7c). Despite being highly enriched, river data had a slope of 8, paralleling the LMWL. This indicates the presence of recent monsoon precipitation in the system. The river at RM 124 and RM 116 were dramatically more enriched than the other sites, indicating that they received isotopically heavy monsoon driven inflow from the Rio Puerco and/or Abo Arroyo (Fig. 3.7e). The drain samples had a trend slope of 6.1, which is consistent with an evaporative trend in a high humidity environment (Clark, 2015). By this point in the season crops and vegetation were vigorous and conditions were saturated due to the monsoon and long-term irrigation, which would increase the humidity in the valley.

During October waters in both the river and drains were enriched and highly clustered (Fig. 3.7f). The RM 124 and RM 116 river samples were more enriched than the rest, likely due to tributary and/or Paleozoic-influenced groundwater inputs. Both the river and the drains had slopes less than 6, indicating they were evaporated. The river was more enriched than the drains during this month, indicating that their source was more evaporated and/or had a larger monsoon component than the drains.

In December  $\delta^{18}\text{O}$  and  $\delta^2\text{H}$  values were moderate and plotted close to the LMWL. (Fig. 3.7f). The river samples were highly clustered, suggesting minimal mixing or evolution occurred during this campaign. The drains returned to near their baseflow values except for RM 124, which was highly enriched. With the exception of RM 124, the return to the LMWL and lighter isotopic signature in the drains while the river remained isotopically heavier suggests that irrigation and monsoon water was flushing from the system and regional groundwater was reestablishing dominance.

River stable isotope data from the project area collected in August of 2001 were similar to the samples collected in August for this study (Fig. 3.7e), and samples from January 2001 were similar to the data that was collected in May (Fig. 3.7a; Fig. 3.7f) for this study (Mills, 2001). The fact that winter river baseflow in 2021 is isotopically heavier than in 2001 may be due to regional drought, which may have evaporated regional baseflow sources. The fact that January 2001 river flows had a similar isotopic composition as snowmelt runoff implies that unevaporated snowmelt was a more volumetrically significant source 20 years prior to this study.

Clear concentration discharge (QC) relationships are not apparent due to the variability of water use practices and dominant water source (snowmelt, monsoon precipitation, tributary inflow, treated wastewater, etc.). This reinforces that the majority of volumetric flow is driven by a relatively dilute source (modern precipitation, irrigation

return flows, treated wastewater) rather than by high TDS groundwater. The exception is surface inflow from certain tributaries (Abo Arroyo, Rio Puerco) which have the capacity to contribute high volumes of meteoric water laden with solute from upland bedrock watersheds.

### 4.3 Mixing Analysis

Sample data was plotted in  $^{87}\text{Sr}/^{86}\text{Sr}$  vs.  $1/[\text{Sr}^{2+}]$ , wherein observations varied significantly with respect to both axes. This variance was best described by the presence of three end-members with distinct  $^{87}\text{Sr}/^{86}\text{Sr}$  and  $[\text{Sr}^{2+}]$  compositions. End-members that circumscribed the data were identified including: flow from the Rio Grande headwaters ( $[\text{Sr}^{2+}] \cong 0.25 \text{ ppm}$ ,  $^{87}\text{Sr}/^{86}\text{Sr} \cong 0.7906$ ; (Hogan et al., 2007), sedimentary (or deeply circulating) brine ( $[\text{Sr}^{2+}] \cong 10.6 \text{ ppm}$ ,  $^{87}\text{Sr}/^{86}\text{Sr} \cong 0.7106$ ; (Burke et al., 1982; Hogan et al., 2007), and water influenced by Paleozoic sediment ( $[\text{Sr}^{2+}] \cong 3 \text{ ppm}$ ,  $^{87}\text{Sr}/^{86}\text{Sr} \cong 0.709$ ; (Mukhopadhyay and Brookins, 1976; Plummer et al., 2004). These endmembers make physical sense in the context of the hydrologic system (Fig. 5.1). Samples collected near regions with high Paleozoic sediment fractions plot towards the Paleozoic endmember, and samples collected where basin geometry supports a vertical component of flow plot towards the brine endmember.

Waters obtain their strontium isotopic content through water-rock interactions, generally mineral dissolution.  $^{87}\text{Sr}/^{86}\text{Sr}$  is stable and does not fractionate and is thus a conservative tracer of water-rock interactions (Clark, 2015). Both  $^{86}\text{Sr}$  and  $^{87}\text{Sr}$  are stable isotopes of Sr, but  $^{86}\text{Sr}$  does not have a radiogenic source, while  $^{87}\text{Sr}$  does.  $^{87}\text{Sr}$  decays from rubidium-87. Rubidium-87 substitutes with potassium and is relatively common in potassium feldspars and, thus, plutonic rocks. Plutonic rocks have high ratio of  $^{87}\text{Sr}$  to  $^{86}\text{Sr}$  due to the radiogenic decay of  $^{87}\text{Rb}$ , as determined by the initial  $^{87}\text{Sr}/^{86}\text{Sr}$  value of the rock, the initial Rb/Sr ratio, and the age rock's age (Land et al., 2000). Conversely, limestones and evaporites have relatively low  $^{87}\text{Sr}/^{86}\text{Sr}$  values due to the absence of Rb both in the mineral and in source water. The characteristic  $^{87}\text{Sr}/^{86}\text{Sr}$  ratio of limestones and evaporites varies as a function of the depositional context and depositional age. With no Rb content, limestones and evaporites inherit the  $^{87}\text{Sr}/^{86}\text{Sr}$  of the water they formed within (Mukhopadhyay and Brookins, 1976) – such as the case of the Paleozoic marine rocks present in the project area. Because of oceanic mixing,  $^{87}\text{Sr}/^{86}\text{Sr}$  values in marine limestones are fairly consistent globally and vary primarily as a function of time. Burke et al. (1982) demonstrated that  $^{87}\text{Sr}/^{86}\text{Sr}$  decreased variably between the Cambrian and Jurassic, and subsequently increased from the Cretaceous to the Quaternary – with average values ranging from  $\sim 0.7068$  to  $0.7091$ . However, inland marine environments (such as the North American Pennsylvanian-Permian epicontinental seas and the Cretaceous Interior Seaway) that are restricted from global mixing can have variable  $^{87}\text{Sr}/^{86}\text{Sr}$  values that deviate from global trends (Mukhopadhyay and Brookins, 1976).

End-member compositions were chosen based on data fit, physical context, and constrained by available data. The  $^{87}\text{Sr}/^{86}\text{Sr}$  ratio of the brine endmember is the highest recorded in the basin (Hogan et al., 2007) although higher values likely exist at depth. The  $^{87}\text{Sr}/^{86}\text{Sr}$  ratio of the Paleozoic-influenced end-member is close to the peak average value of seawater from throughout Phanerozoic time and higher than typical values of seawater during the Paleozoic (Burke et al., 1982) in order to reflect the partially restricted depositional setting during that period, wherein marine deposits would contain a higher

proportion of high  $^{87}\text{Sr}/^{86}\text{Sr}$  continental weathering products than the global average (Mukhopadhyay and Brookins, 1976). Williams et al., (2013) documented a spring associated with Paleozoic rock and sediment at the southeastern edge of the basin with an  $^{87}\text{Sr}/^{86}\text{Sr}$  value of 0.7090, which provides confidence to the use of this value. The average  $^{87}\text{Sr}/^{86}\text{Sr}$  value of seawater was lower during the Cretaceous, so contributions from water that interacted with Cretaceous marine sediments (which comprise much of the upper Rio Puerco watershed) would not be expected to increase the  $^{87}\text{Sr}/^{86}\text{Sr}$  of Puerco flow. Cretaceous-influenced water present in the system is thus included in the Paleozoic end-member.

Water-rock interactions impart the  $^{87}\text{Sr}/^{86}\text{Sr}$  signature of host rock to natural waters, however the rate at which a water assimilates with a whole rock  $^{87}\text{Sr}/^{86}\text{Sr}$  value is dependent on the dissolution rate of individual minerals and individual mineral's  $^{87}\text{Sr}/^{86}\text{Sr}$  values. Whole rock  $^{87}\text{Sr}/^{86}\text{Sr}$  values of Precambrian granites have  $^{87}\text{Sr}/^{86}\text{Sr}$  values of near 0.75. K-feldspar and potassium phyllosilicate minerals have  $^{87}\text{Sr}/^{86}\text{Sr}$  values much higher than the whole rock average, while plagioclase feldspars are lower (McNutt, 2000). Plagioclase – particularly anorthite – has a high dissolution rate and can initially impart a low  $^{87}\text{Sr}/^{86}\text{Sr}$  signature to waters. With greater residence time, plagioclase and K-feldspar can equilibrate and increase the  $^{87}\text{Sr}/^{86}\text{Sr}$  of groundwater (Frost and Toner, 2004). Groundwater with long residence time in felsic aquifers – such as sedimentary brines – can acquire  $^{87}\text{Sr}/^{86}\text{Sr}$  signatures approaching the whole-rock value, while groundwater moving along shorter flow paths will remain low. When water is undersaturated with respect to them carbonate minerals, the  $^{87}\text{Sr}/^{86}\text{Sr}$  dissolved in the water can approach that of the carbonate host rocks quickly – potentially in only a matter of days (Frost and Toner, 2004). Waters analyzed in this project were significantly undersaturated with respect to anorthite (SI ~ -7), supersaturated in respect to K-feldspar (SI ~ 1) and variably saturated with muscovite (SI ~ 0.8; Figure ). Assuming that biotite (which is very radiogenic) behaves similarly to muscovite, we can infer that anorthite significantly mediates the overall  $^{87}\text{Sr}/^{86}\text{Sr}$  signature.

The validity of this method of analysis is dependent on the chosen end-member compositions. Of these, the brine composition is the most uncertain as no direct samples of the deepest brines are available. We have used established estimates to provide consistency with other studies (e.g. Hogan et al., 2007). Because upwelling brine will become diluted with shallower waters before reaching the surface, the fraction of non-riparian basin groundwater present in the drains will be higher than the fraction of brine indicated, implying that the significance of non-riparian or Paleozoic influence groundwater is greater than otherwise suggested.

The percent contributions of Rio Grande headwaters, sedimentary brine, and water that interacted with Paleozoic strata/sediment determined in a given sample are presented in and Table 4.1. By this method, brine fractions in the were as high as 4% in the RM 141 drain, 2% in the RM 155, 135, and 124 drains, and 1% in the RM 165 drain. The brine fraction in the river at San Acacia (RM 116) were as high as 1%. Paleozoic-influenced waters were as high as 21% in the RM 124 drain, 17% in the RM 141 drain, 11% in the RM 135 drain, 7% in the RM 155 drain, 6% in the RM 165 drain, and 14% in the river at San Acacia (RM 116).

We present the mixing model results graphically in Figure 4.1 with a fixed  $^{87}\text{Sr}/^{86}\text{Sr}$  and strontium concentration for the end-members. However, the strontium chemistry of the

river entering the project area (RM 165) was quite variable over the year. To understand how this variability impacts mixing model uncertainty, calculations were also performed using  $^{87}\text{Sr}/^{86}\text{Sr}$  and  $[\text{Sr}^{2+}]$  measured in the river at the upstream end of the project as the river endmember for the corresponding campaign. (Table 4.1). This approach reduced the apparent brine contributions, but did not qualitatively change our interpretation.

We believe that the variability in the upstream  $^{87}\text{Sr}/^{86}\text{Sr}$  value is due largely in part to Albuquerque shifting its municipal water source from surface water to groundwater in between mid-June and mid-November, and then back to surface water from mid-November into December. During this interval, water was pumped from municipal supply wells throughout the city, used domestically and commercially, treated, and then discharged immediately north of the project area at a rate of  $\sim 1.1 \text{ m}^3/\text{s}$  (Fig. 1.5a). During the months of August and September ABCWA discharge was a principal component of total river flow in addition to intermittent monsoon inputs, and it remained a significant component of flow throughout the month of October (Fig. 1.5b). The diversion point for irrigation water used throughout the entire project area is at the Isleta Diversion Weir – just upstream of the northernmost sample location (Fig. 1.5c). Thus, water used for irrigation during this period would have a similar  $^{87}\text{Sr}/^{86}\text{Sr}$  to the river's upstream value. This value would also be preserved in irrigation return flows due to the conservative nature of the  $^{87}\text{Sr}/^{86}\text{Sr}$  ratio.

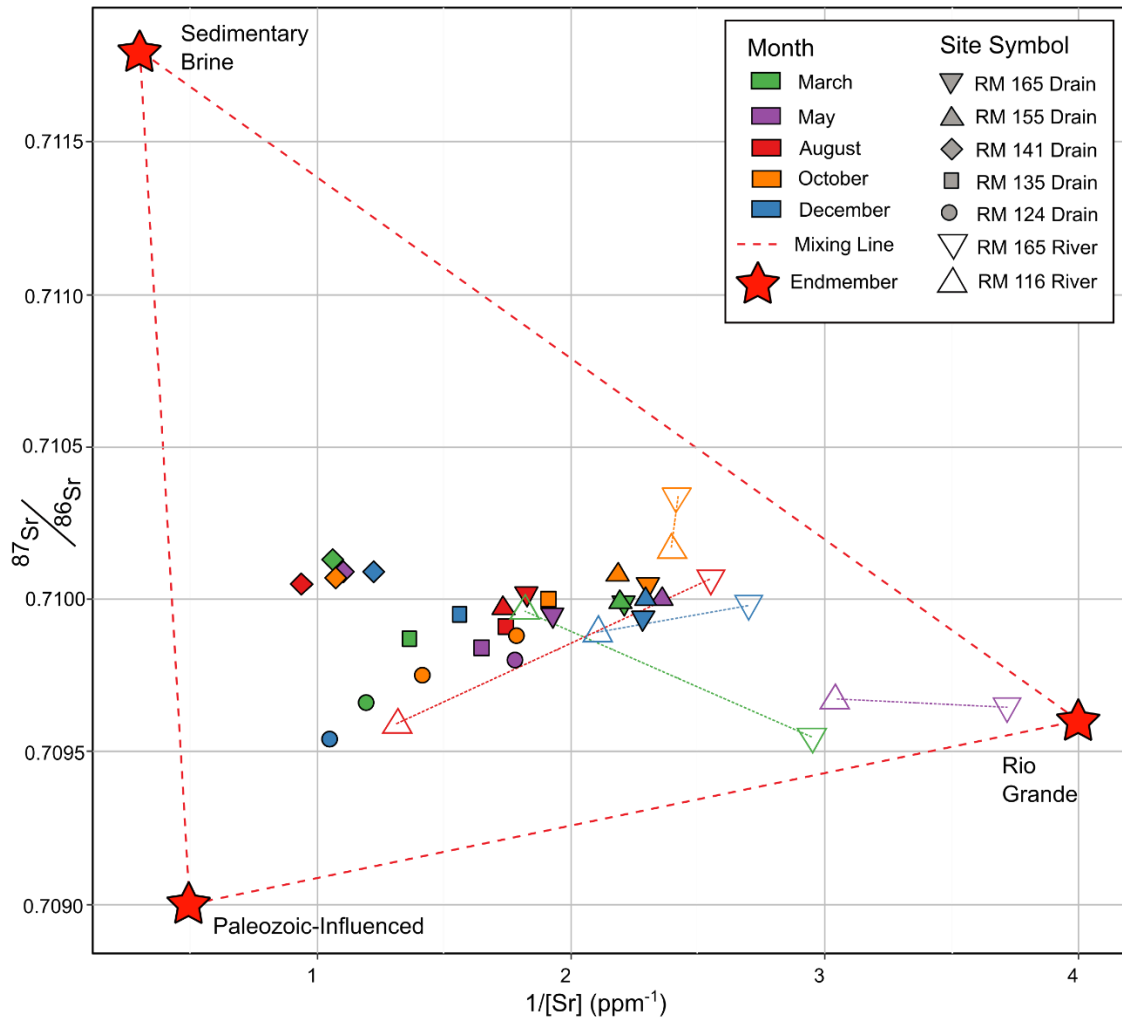


Figure 4.1. Samples and endmembers in  $1/[Sr]$  vs.  $^{87}Sr/^{86}Sr$  mixing space. Dashed lines correspond to 1:1 mixing lines between end-members. River samples for a given month are connected by dotted lines.

The mixing of natural surface water and used-and-treated groundwater into the river introduces uncertainty on many levels. On one hand, the presence of Albuquerque groundwater in the system could lead to overestimations in the determined brine fraction if using the average Rio Grande headwaters  $^{87}Sr/^{86}Sr$  to perform the calculations. Similarly, the proportion of Rio Grande water present could be misestimated if using the value introduced by Albuquerque's groundwater. The best approach for a given site depends on the local timing, rate, and volumetric significance of Albuquerque groundwater influenced irrigation return flows. According to MRGCD gauge records, approximately  $6.2 \times 10^7$  m<sup>3</sup> of water (~50,000 acre-feet) was diverted for irrigation in the project area between mid-June and mid-November. The majority of this water would be evapotranspired, but assuming 25% of that water becomes irrigation return flow, Albuquerque Groundwater influenced irrigation water would account for about 10 cm of recharge. This water might be flushed out of the system relatively quickly (weeks to months) but is difficult to account for.



Although problematic, the Albuquerque groundwater influenced irrigation water in and of itself provides insight into the timing of irrigation return flows. From Figure , we see that  $^{87}\text{Sr}/^{86}\text{Sr}$  values in the drains are fairly consistent between May and August despite irrigation with Albuquerque influenced groundwater having been ongoing for some time – although Albuquerque groundwater made up a variable fraction of flow leading up to this campaign (Fig. 1.5). However, by October an overall increase in the drain  $^{87}\text{Sr}/^{86}\text{Sr}$  was apparent. By December the northern two drains had shifted back to their background values, the RM 135 drain shifted to a median value, and the RM 124 drain dropped to the lowest  $^{87}\text{Sr}/^{86}\text{Sr}$  of the campaign – presumably due to a high fraction of Paleozoic-influenced groundwater (Table 4.1). The general trend in  $^{87}\text{Sr}/^{86}\text{Sr}$  described above is also apparent in nitrate, which is primarily contributed to the system by wastewater effluent (Oelsner et al., 2007).

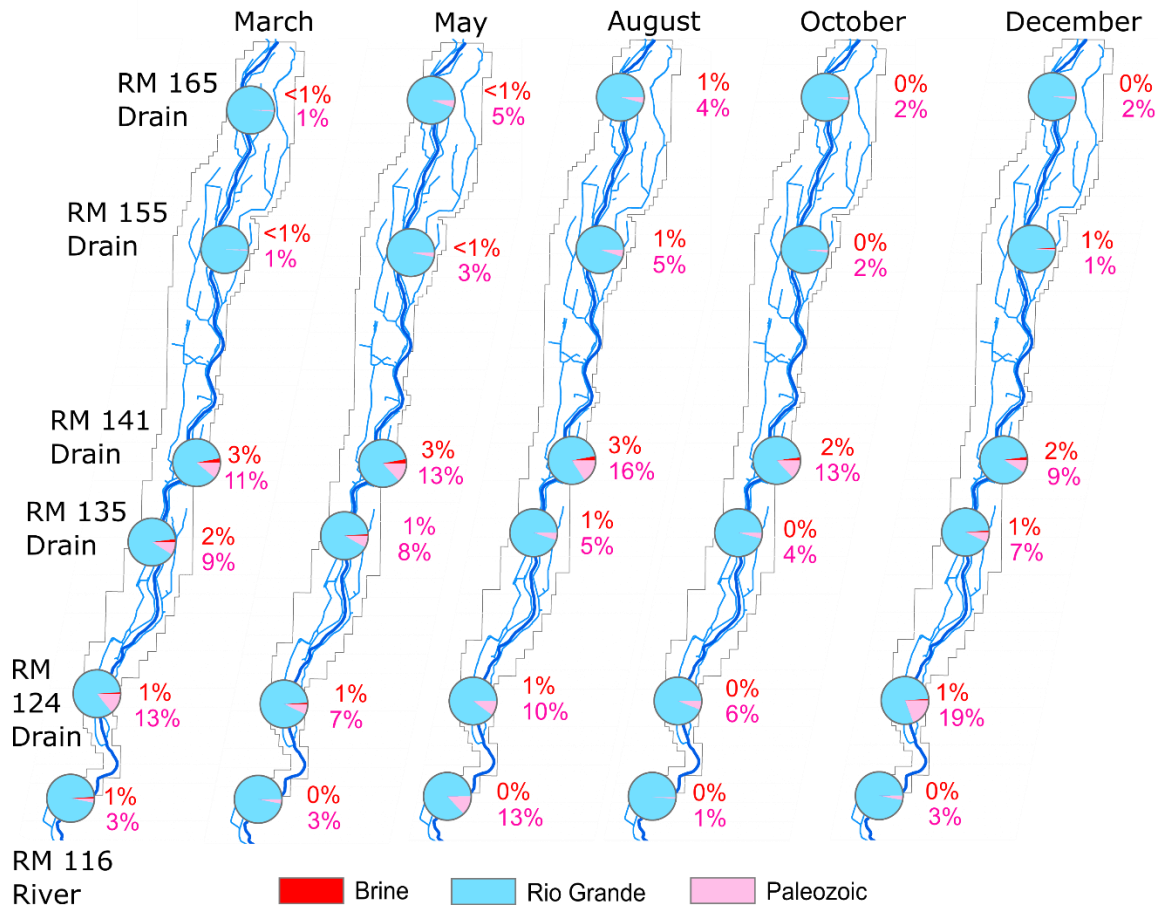


Figure 4.2. Spatial distribution of mixing fractions as determined by the upstream river composition as the Rio Grande end member. Composition and location are given by pie chart.

The two northernmost sites (RM 165 and RM 155) behaved similarly to each other. Neither of them had a significant brine fraction except during August, when they were affected by Albuquerque groundwater (The fraction is corrected when adjusting the river endmember value; Table 4.1). Confusingly, both sites had a measurable Paleozoic fraction throughout the year despite being far north of major Paleozoic influenced tributary systems

and associated groundwater zones. This observation is best explained by evaporation, which leads to an increase in strontium concentration without affecting the  $^{87}\text{Sr}/^{86}\text{Sr}$  ratio. The conductivity and chloride concentrations were higher in the drains than the river at these sites, supporting the likelihood of evaporation. Thus, it is reasonable to assume that Paleozoic water was not in fact present.

The RM 141 drain behaved differently from the other drains. Its  $^{87}\text{Sr}/^{86}\text{Sr}$  value decreased during the height of irrigation season despite the presence of the radiogenic Albuquerque groundwater. In other drains, the increased head in the shallow aquifer and drains from irrigation likely suppressed or swamped-out the upwelling sedimentary brines. However, for RM 141 this conclusion is directly contradicted by the calculated percentage of brine which was highest in August (4%). This contradiction could be due to the high overall strontium concentration during this month due to an influx of Paleozoic-influenced water (17%), which could skew the calculation. Supporting evidence for a high brine fraction at this site is given by the presence of elevated trace metals. Uranium ranged from 6.0-8.6 ppb in the RM 141 drain, while the 2.5 ppb was the highest value recorded at any other site. Barium, boron, and lithium were also elevated with respect to other sites (Fig. 3.6) Evidence for upwelling sedimentary brine that is in the middle of the a basin and not associated with a fault or volcanic feature has thus far not been reported in the literature, and fits poorly with previous conceptual models.

However, the presence of a high brine fraction in the RM 141 drain makes physical sense in the context of the basin geometry. Figure 1.2 shows that the RM 141 site is located above a bedrock high juxtaposed against a deep ‘trough’ of basin fill within the Hubble Half-Graben (Grauch and Connell, 2013). From the groundwater contours in Figure 1.4 we see that direction of historical groundwater flow aligns with this ‘trough’. From this evidence, we posit that deep basin flow paths within the ‘trough’ are forced upwards in the vicinity of the RM 141. This conclusion follows the same logic behind the axial deep basin flow path theory (Phillips et al., 2003; Hogan et al., 2007) but demonstrates that the process can be caused by localized, buried basin structure that strikes parallel to the riparian system, not just Quaternary faulting cutting sub-normally to the river or regional scale basin boundaries.

The RM 135 site was variable throughout the year, ranging from a 1-2% brine fraction and a 5-11% Paleozoic fraction. These higher fractions make sense given the site’s proximity to the basin’s terminus and the Paleozoic tributaries (Fig. 4.1). Surprisingly, the Paleozoic fraction was lowest in August and October, where monsoon rains could be expected to increase the influence the influence of the tributaries on the system. Because the RM 135 site is (1) above the confluence of the Rio Puerco and the Rio Puerco Hydrogeochemical groundwater (Fig. 1.4), and (2) on the opposite side of the Rio Grande as Abo Arroyo – it is possible that this site was shielded from the influence of the monsoon, and the higher fractions of Paleozoic water during baseflow conditions are due to Paleozoic-influenced groundwaters becoming more dominant in the absence of irrigation-driven head gradients. The Abo Arroyo Hydrogeochemical zone perhaps becomes dominant even though it is on the other side of the river (Fig. 1.4). A potential source of water is from the the axis of the basin (Fig. 1.2), which underlies the groundwater ‘trough’ west of the river (Fig. 1.4). It is possible that the basin axis depocenter has a high proportion of sediment derived from Paleozoic/Mesozoic uplands given its proximity to the western edge of the basin. If this is the case, waters at depth that would be considered sedimentary

brines may have a lower  $^{87}\text{Sr}/^{86}\text{Sr}$  ratio than expected, making it's contribution difficult to resolve in the current mixing model.

The RM 124 site had the most overall variability and the highest fractions of Paleozoic influenced water (7-21%). This is not surprising given that this site has 120.6 km of contributing upstream drains and is located immediately downstream of the Rio Puerco confluence and is on the same side of the Rio Grande. However, brine fraction is relatively absent (just 1-2%), an unexpected result considering its proximity to the basin terminus. Moreover, this site is at an approximately equal elevation to the river in an area of the basin that is typically a gaining system. That said, this site is located within the Rio Puerco Hydrogeochemical Zone (Fig. 1.4) rather than the Discharge zone – where the majority of brine inputs are thought to occur (Phillips et al., 2003; Plummer et al., 2004).

The Rio Grande at RM 116 (San Acacia) is a difficult site to interpret due to the presence of the San Acacia Spring System, which contributes mantle-sourced water (evidenced by Helium isotopes) with a high strontium concentration and overall salinity but fairly low  $^{87}\text{Sr}/^{86}\text{Sr}$  ratio ( $\sim 0.7098$ ) to the system along major faults (Williams et al., 2013). The influence of this spring cannot be resolved in our mixing model because its  $^{87}\text{Sr}/^{86}\text{Sr}$  value is not extreme relative to the other endmembers present. Contributions from the spring may in fact obfuscate the relative abundance of the other endmembers. Using the monthly RM 165 Rio Grande value as the river endmember is most appropriate for this site – and per these calculations the only month with a measurable brine component was March (1%). The role of Paleozoic-influenced water is easier to interpret than the influence of basin brine. These contributions ranged from 1-13%, peaking in August when monsoon flows were a major component of flow. During baseflow conditions in March, Paleozoic contributions were 3% despite the absence of tributary flow. This amounts to a gross discharge of about  $0.5 \text{ m}^3/\text{s}$  ( $\sim 18 \text{ CFS}$ ) of Paleozoic-influenced groundwater. This is comparable to December, suggesting the winter Paleozoic-endmember baseflow component is fairly consistent.

		Brine	Rio Grande	Paleo.	Brine	Rio Grande	Paleo.	
Riverside Drain	RM 165	March	1%	95%	4%	1%	98%	1%
		May	1%	93%	5%	1%	94%	5%
		August	2%	93%	6%	1%	96%	4%
		October	1%	96%	3%	0%	98%	2%
		December	1%	96%	3%	0%	98%	2%
	RM 155	March	1%	95%	4%	1%	98%	1%
		May	1%	96%	3%	1%	97%	3%
		August	2%	92%	7%	1%	95%	5%
		October	1%	96%	3%	0%	98%	2%
		December	1%	96%	3%	1%	98%	1%
	RM 141	March	3%	83%	13%	3%	86%	11%
		May	3%	84%	13%	3%	84%	13%
		August	4%	80%	17%	3%	82%	16%
		October	3%	83%	14%	2%	85%	13%
		December	3%	86%	11%	2%	89%	9%
	RM 135	March	2%	87%	11%	2%	90%	9%
		May	1%	90%	8%	1%	91%	8%
		August	1%	92%	7%	1%	94%	5%
		October	1%	94%	5%	0%	96%	4%
		December	2%	90%	8%	1%	92%	7%
	RM 124	March	2%	83%	16%	1%	85%	14%
		May	1%	92%	7%	1%	92%	7%
		August	1%	87%	12%	1%	89%	10%
		October	1%	92%	7%	0%	94%	6%
		December	1%	78%	21%	1%	80%	19%
Rio Grande	RM 165	March	1%	94%	5%	Used as Rio Grande end-member		
		May	0%	100%	0%			
		August	1%	97%	2%			
		October	1%	98%	1%			
		December	1%	97%	2%			
	RM 116	March	1%	93%	6%	1%	96%	3%
		May	0%	98%	2%	0%	98%	2%
		August	1%	84%	15%	0%	87%	13%
		October	1%	97%	2%	0%	99%	1%
		December	1%	94%	5%	0%	97%	3%
		Rio Headwater EM values			Monthly River EM values			

Table 4.2. Table of end-member fractions by [Sr] vs.  $^{87}\text{Sr}/^{86}\text{Sr}$  mass balance calculations. Data on the left uses a fixed Rio Grande endmember composition. Data on the right uses the measured upstream Rio Grande composition from a given month as that month's river endmember.

## CHAPTER 5

### CONCLUSION

#### 5.1 Overview

We present a conceptual model of groundwater flow in the basin that is composed of three major end-members: water from the Rio Grande, deep upwelling sedimentary brine, and water associated with southern basin tributary systems that interact with Paleozoic rocks and sediment. The distribution of these flow paths are shown in Figure 5.1. Rio Grande water is volumetrically dominant in the riparian aquifer and surface waters, which are interconnected. Rio Grande water flows down the axis of the basin and is distributed into the riparian aquifer through direct channel seepage and irrigation. Sedimentary brine flow is driven by gravity along the deepest parts of the basin and is locally forced upwards by the geometry of the basin. It is a volumetrically minor component of flow but contributes a high proportion of solute to the shallow system in localized areas. Paleozoic-influenced waters are associated with southern basin tributaries that drain regions with exposed Paleozoic strata, principally the Los Pinos/Manzano mountains and the Lucero Uplift. These waters can account for a measurable volumetric component of surface flows and threaten water quality.

Our results demonstrate (1) Paleozoic-influenced waters comprise a significant component of flow and are a major solute source, (2) upwelling sedimentary brine is driven by basin structural controls and is not constrained to the lowermost basin, and (3) seasonal variability and anthropogenic factors control mixing behavior and influence geochemical trends, specifically for the shallow aquifer. The first two conclusions have not previously received much recognition in the literature and build on our scientific understanding of the transient, three-dimensional nature of how water and solute travels through the Albuquerque basin. While the first point is locally relevant to the Albuquerque Basin, it demonstrates that tributary systems may exert a major control on water quality and quantity even – even if tributary surface discharge is minor—which is a vital observation for interpreting groundwater flow in other extensional basins. The second point has broad implications for conceptualizing flow in structurally complex, extensional basins in general. The specifics of the third conclusion are relevant to the scientific understanding of the basin and provide practical utility for water users and managers.

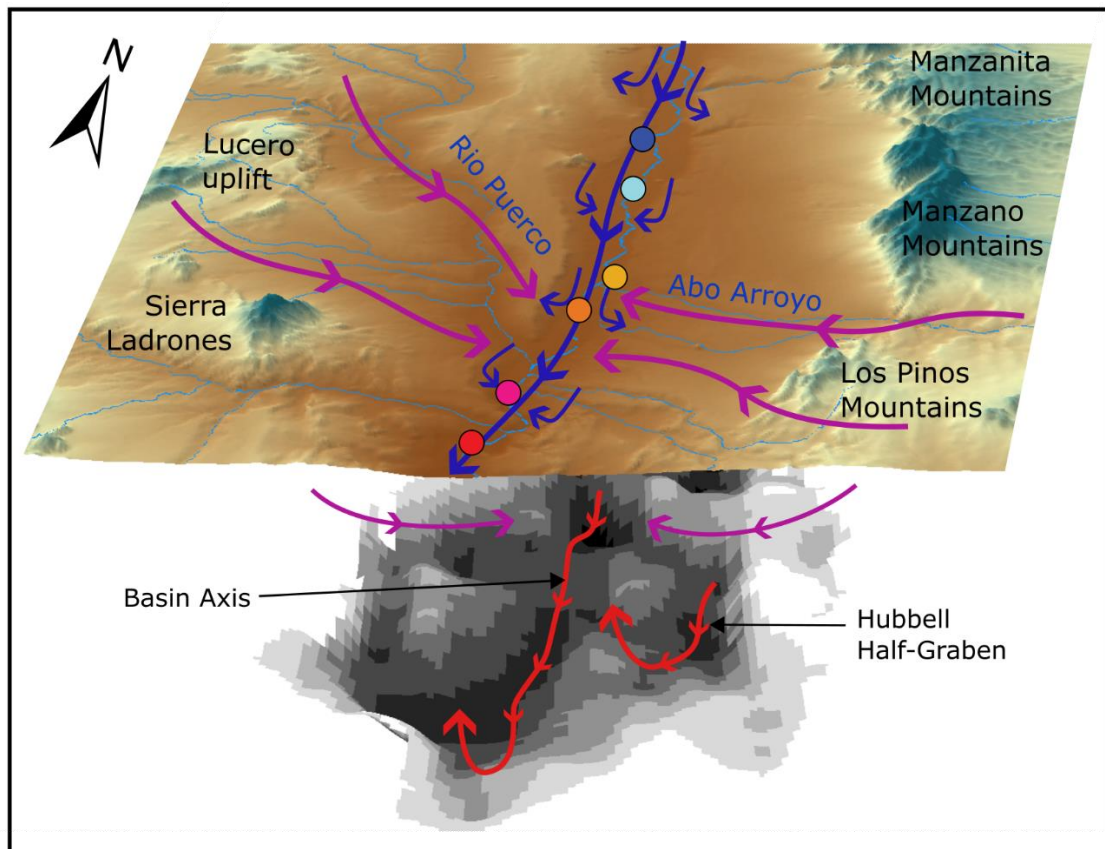


Figure 5.1. 3-D basin fill thickness (Grauch and Connell, 2013) and surface topography of the southern Albuquerque basin showing the site locations and interpreted flow path distribution of end-member waters identified in this study.

Flows of the Rio Grande entering the study area can include snowmelt runoff from the Rocky Mountains, monsoon precipitation, and municipal discharge. Although the upstream sources of Rio Grande flow are variable, Rio Grande flow entering the project area is characteristically dilute and suitable for beneficial use. Water from the Rio Grande is the primary recharge source to the basin, entering the basin aquifer system through channel seepage and as irrigation return flows. River stage and irrigation practices dictate

the extent to which recharge occurs, thus climatic and anthropogenic factors exert a first order control on the system. Groundwater exchanges between the river and the riparian aquifer are driven by the gradient between the river and the riverside irrigation drains, as well as by regional groundwater flow gradients.

Paleozoic-influenced waters are recognized to include surface flows and associated groundwater zones of the Rio Puerco and Abo Arroyo, but may also include waters of the Western Boundary groundwater zone. These waters are variable in composition and are less solute laden than sedimentary or mantle brines. However, they are high in sulphate and chloride – both of which significantly degrade water quality. The risk posed by these waters was captured in the RM 124 drain during December, where a contribution of 21% Paleozoic-influenced water resulted in a sulphate of concentration of 234 ppm, chloride concentration of 131 ppm – and a specific conductance of 1223  $\mu\text{S}/\text{cm}$ . This would be considered unacceptable to drink, and is only marginally appropriate for irrigation. Water in this drain is sometimes directly channeled into the Socorro irrigation network – presenting a unique risk to downstream users. With additional solute contributions from brine sources combined with evaporative concentration, these waters are a significant concern. The presence of these waters may have also resulted in overestimation of sedimentary brine's role in overall river salinization.

Evidence for upwelling brine near RM 141 includes elevated trace metals and a high  $^{87}\text{Sr}/^{86}\text{Sr}$  ratio. Mixing calculations determined the brine fraction to be as much as 4% at this location. We conclude that the brine is of a sedimentary source, and is driven to the surface by gravity driven flow forced upwards by basin geometry. This basic principle has been explored by several authors but was thought to occur principally at basin termini (Hogan et al., 2007; Phillips et al., 2003). Although RM 141 is towards the southern end of the basin, it is well above the terminus and is located above the discharge groundwater zone where the majority of groundwater mixing is thought to occur (Plummer et al., 2004, Williams et al., 2013). Brine fractions at this location were in fact the highest observed in the study. The presence of mid-basin brines has been previously identified in the rift but is typically associated with fault systems and has a geothermally component (Williams et al., 2013) – for which there is no evidence of in this case. The relationship between basin structure and the shallow groundwater system is not typically considered, but this evidence stresses that this relationship can be significant and should be further explored.

Seasonality and water use practices have the greatest control on the chemistry and flow dynamics of the system. While this is intuitive, the extent of these changes have not previously been quantified in the Albuquerque Basin in this manner. Trends can be broken into four major periods throughout the year: winter baseflow, spring runoff, irrigation season, and re-equilibration. The greatest increase in salinity occurs during winter baseflow. Upwelling sedimentary brine has the highest fraction during this period, and a high fraction of Paleozoic-influenced water is also present. This period can be considered steady state due to consistent river flows and an absence of irrigation. The Rio Grande is broadly a gaining reach throughout the project area during this time. Upon spring runoff, high flows of dilute water flush the system and suppress the signal of Paleozoic-influenced waters and brines. Not only are these contributions diluted by high flows, their input volumes are presumably limited by an increase in head in the riparian aquifer (as evidenced by higher drain discharge). Minimal chemical evolution of surface waters occurs during this time. A majority of recharge likely occurs during and before this period, as evidenced

by the light isotopic composition of the river compared with the isotopic composition of the northern drains (Fig. 4.8) During the irrigation season, water is subjected to a litany of environmental and anthropogenic forcings and the chemistry of the system becomes highly variable. Perturbations to the system during this period include (1) changes in source of water to the system (monsoon rains, tributary flows, groundwater pumped by Albuquerque and discharged into the river), (2) high evaporation rates, (3) irrigation and the associated evapotranspiration and soil-water interactions, and (4) an overall reduction of river flow, and even intermittent drying of the river. During the irrigation period, waters exhibit enriched isotopic signatures characteristic of evaporation and have variable ion proportions due to source variability and increased ion exchange opportunities. In the absence of mixing, waters maintain a moderate but overall stable solute load. Paleozoic-influenced water (largely driven by monsoon flows and surface runoff) is the highest mixing component during this period. In the re-equilibration phase, irrigation return flows are flushing out of the system while the Rio Grande re-establishes stable flow. Irrigation return flows into the Rio Grande create a variable river composition, while conditions stabilize elsewhere in the aquifer.

## **5.2 Management recommendations**

1. Paleozoic-influenced groundwater is present in greater abundance in the vicinity of Abo Arroyo and the Rio Puerco. The Unit no. 7 drain in particular will accumulate flow from this source. It may be advisable to mix water from the Rio Grande with Unit No.7 Drain water – a conductivity meter could be installed to better account for this risk.
2. The evaporation of ponded water in the La Joya vicinity can increase the salinity risk to groundwater and surface water resources due to the high salinity of the groundwater present. A supply of low conductivity water (early season diversions) may help manage salt accumulation in the area
3. It is unrealistic to install interception wells to sequester Paleozoic-influenced groundwater, and a specific location to intercept upwelling sedimentary brine was not identified in this study. However, the possibility of installing an interception well in the vicinity of the San Acacia Spring could have a measurable impact on downstream water quality if the need arises in the future.
4. Discharge from the ABCWA water treatment plant can be chemically traced throughout the MRGCD Belen District and can be the dominant source of water to the system when river flows are low.



## CONCLUDING REMARKS

- Paleozoic-influenced waters are volumetrically significant in the southern portion of the basin in the vicinity of Abo Arroyo and Rio Puerco. Inflow from these waters pose a water quality risk.
- Sedimentary brine inflows are present in the distal basin and near Highway 346 (River Mile 141). Sedimentary brine only appears to affect the river in the distal basin. The fraction of sedimentary brine is greatest during pre-irrigation season during winter baseflow.
- $\text{Na}^+/\text{Ca}^{2+}$ ,  $(\text{Cl}^- + \text{SO}_4^{2-}/\text{HCO}_3^-)$ ,  $[\text{Cl}^-]$ , and specific conductivity all generally increase with flow distance.
- Chloride mass flux was highest in the river March and December and increased throughout the project area. Chloride mass flux was fairly stable in the river during May, August, and October. Evidence of chloride ‘flushing’ was not observed in the drains or river.
- Irrigation return flows could not be quantitatively accounted for, but the timing of irrigation return water was qualitatively observed using  $^{87}\text{Sr}/^{86}\text{Sr}$ ,  $\delta^{18}\text{O}$  and  $\delta^2\text{H}$ . Irrigation return flows were abundant in the drains by October, and were mostly flushed by December.
- End Member Mixing Analysis (see electronic supplement) was attempted but end member identification was unsuccessful due to the number of significant principal components determined. End Member Mixing Analysis may be successful if more conservative tracers are employed.
- Dilution gauging is not appropriate when turbidity is high. Conventional gauging was generally successful. Differential gauging in the project area should be performed at kilometer scale intervals in order to obtain statistically significant volumetric inflow measurements.
- The groundwater inflow rates determined from radon activity are the most accurate inflow rates reported in this study, however future studies using this method should determine site specific gas transfer velocities following Cook (2013) to improve the accuracy of this measurement.
- Discharge of Albuquerque groundwater into the river from the Albuquerque Wastewater treatment plant increases the strontium isotopic ratio of the river.

## References

- Bexfield, L.E., Anderholm, S.K., 2000. Predevelopment water-level map of the Santa Fe Group aquifer system in the middle Rio Grande basin between Cochiti Lake and San Acacia, New Mexico, Water Resources Investigations Report 00-4249. <https://doi.org/10.3133/wri004249>
- Bexfield, L.E., Heywood, C.E., Kauffman, L.J., Rattray, G.W., Vogler, E.T., 2011. Hydrogeologic Setting and Groundwater Flow Simulation of the Middle Rio Grande Basin Regional Study Area, New Mexico (Professional Paper No. 1737-B), Professional Paper.
- Burke, W.H., Denison, R.E., Hetherington, E.A., Koepnick, R.B., Nelson, H.F., Otto, J.B., 1982. Variation of seawater  $^{87}\text{Sr}/^{86}\text{Sr}$  throughout Phanerozoic time. *Geology* 10, 516. [https://doi.org/10.1130/0091-7613\(1982\)10<516:VOSSTP>2.0.CO;2](https://doi.org/10.1130/0091-7613(1982)10<516:VOSSTP>2.0.CO;2)
- Clark, I., 2015. Groundwater Geochemistry and Isotopes 442.
- Connell, S.D., 2001. Stratigraphy of the Albuquerque Basin, Rio Grande Rift, Central New Mexico: A Progress Report. NMBGMR OFR-454B 28.
- Cook, P.G., 2013. Estimating groundwater discharge to rivers from river chemistry surveys: GROUNDWATER DISCHARGE TO RIVERS. *Hydrol. Process.* 27, 3694–3707. <https://doi.org/10.1002/hyp.9493>
- Cook, P.G., Favreau, G., Dighton, J.C., Tickell, S., 2003. Determining natural groundwater influx to a tropical river using radon, chlorofluorocarbons and ionic environmental tracers. *J. Hydrol.* 277, 74–88. [https://doi.org/10.1016/S0022-1694\(03\)00087-8](https://doi.org/10.1016/S0022-1694(03)00087-8)
- Eash, N.S., 2016. Soil science simplified, Sixth edition. ed. John Wiley & Sons, Inc, Hoboken, New Jersey.
- Essington, M.E., 2004. Soil and water chemistry: an integrative approach. CRC Press, Boca Raton.
- Frost, C.D., Toner, R.N., 2004. Strontium Isotopic Identification of Water-Rock Interaction and Ground Water Mixing. *Ground Water* 42, 418–432. <https://doi.org/10.1111/j.1745-6584.2004.tb02689.x>
- Gangopadhyay, S., McGuire, M., Martin, J., Pederson, G., Woodhouse, C., Littell, J., Mizukami, N., Vano, J., Gutmann, E., Wood, A., Devineni, N., Lall, U., Barrett, L., Butler, A., Cameron, J., Estep, M., Fennema, S., Johnson, J., Khaya, J., Llewellyn, D., Parker, N., Prairie, J., Huntington, J., Pearson, C., Broman, D., Spears, M., Tillman, F., 2021. West-Wide Climate and Hydrology Assessment 423.
- Garcia, S., Louvat, P., Gaillardet, J., Nyachoti, S., Ma, L., 2021. Combining Uranium, Boron, and Strontium Isotope Ratios ( $^{234}\text{U}/^{238}\text{U}$ ,  $\delta^{11}\text{B}$ ,  $^{87}\text{Sr}/^{86}\text{Sr}$ ) to Trace and Quantify Salinity Contributions to Rio Grande River in Southwestern United States. *Front. Water* 2, 575216. <https://doi.org/10.3389/frwa.2020.575216>
- Gillentine, J.M., 1996. Petrology and Diagenesis of the Middle and Lower Santa Fe Group in the Northern Albuquerque Basin, New Mexico (No. OFR-402c), NMBGMR.

- Grauch, V.J.S., Connell, S.D., 2013. New perspectives on the geometry of the Albuquerque Basin, Rio Grande rift, New Mexico: Insights from geophysical models of rift-fill thickness, in: *New Perspectives on Rio Grande Rift Basins: From Tectonics to Groundwater*. Geological Society of America. [https://doi.org/10.1130/2013.2494\(16\)](https://doi.org/10.1130/2013.2494(16))
- Hall, J.S., Mozley, P., Davis, J.M., Roy, N.D., 2004. Environments of Formation and Controls on Spatial Distribution of Calcite Cementation in Plio-Pleistocene Fluvial Deposits, New Mexico, U.S.A. *J. Sediment. Res.* 74, 643–653. <https://doi.org/10.1306/020904740643>
- Hogan, J.F., Blum, J.D., Siegel, D.I., Glaser, P.H., 2000.  $^{87}\text{Sr}/^{86}\text{Sr}$  as a tracer of groundwater discharge and precipitation recharge in the Glacial Lake Agassiz Peatlands, northern Minnesota. *Water Resour. Res.* 36, 3701–3710. <https://doi.org/10.1029/2000WR900233>
- Hogan, J.F., Phillips, F.M., Mills, S.K., Hendrickx, J.M.H., Ruiz, J., Chesley, J.T., Asmerom, Y., 2007. Geologic origins of salinization in a semi-arid river: The role of sedimentary basin brines. *Geology* 35, 1063. <https://doi.org/10.1130/G23976A.1>
- Land, M., Ingri, J., Andersson, P.S., Öhlander, B., 2000. Ba/Sr, Ca/Sr and  $^{87}\text{Sr}/^{86}\text{Sr}$  ratios in soil water and groundwater: implications for relative contributions to stream water discharge. *Appl. Geochem.* 15, 311–325. [https://doi.org/10.1016/S0883-2927\(99\)00054-2](https://doi.org/10.1016/S0883-2927(99)00054-2)
- Magnuson, M.L., Valdez, J.M., Lawler, C.R., Nelson, M., Petronis, L., 2019. New Mexico Water Use By Catagories 2015, Technical Report 55. New Mexico Office Of The State Engineer.
- McNutt, R.H., 2000. Strontium Isotopes. *Environ. Tracers Subsurf. Hydrol.* Chapter 8, 233–260.
- Mukhopadhyay, B., Brookins, D.G., 1976. Strontium isotopic composition of the Madera Formation (Pennsylvanian) near Albuquerque, New Mexico. *Geochim. Cosmochim. Acta* 40, 611–616. [https://doi.org/10.1016/0016-7037\(76\)90107-1](https://doi.org/10.1016/0016-7037(76)90107-1)
- Nelson, J.W., Holmes, L.C., Eckmann, E.C., 1914. Soil Survey of the Middle Rio Grande Valley Area, New Mexico.
- Oelsner, Gretchen & Brooks, Paul & Hogan, James. (2007). Nitrogen Sources and Sinks Within the Middle Rio Grande, New Mexico1. *JAWRA Journal of the American Water Resources Association*. 43. 850 - 863. [10.1111/j.1752-1688.2007.00071.x](https://doi.org/10.1111/j.1752-1688.2007.00071.x).
- Phillips, F.M., Mills, S., Hendrickx, M.H., Hogan, J., 2003. Environmental Tracers Applied to Quantifying Causes of Salinity in Arid-Region Rivers: Preliminary Results from the Rio Gra... *Dev. Water Sci.* 50, 327–334. [https://doi.org/10.1016/S0167-5648\(03\)80029-1](https://doi.org/10.1016/S0167-5648(03)80029-1)
- Plummer, L.N., Bexfield, L.E., Anderholm, S.K., Sanford, W.E., Eurybiades, B., 2004. Geochemical characterization of ground-water flow in the Santa Fe Group aquifer system, Middle Rio Grande Basin, New Mexico, Water-Resources Investigations Report 03-4131. <https://doi.org/10.3133/wri034131>
- Ricketts, J.W., Karlstrom, K.E., Priewisch, A., Crossey, L.J., Polyak, V.J., Asmerom, Y., 2014. Quaternary extension in the Rio Grande rift at elevated strain rates recorded in travertine deposits, central New Mexico. *Lithosphere* 6, 3–16. <https://doi.org/10.1130/L278.1>

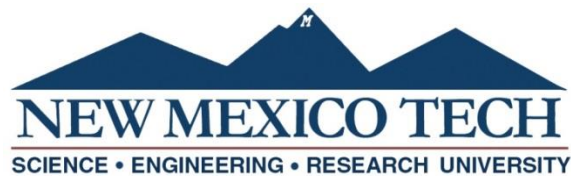
- Roybal, F.E., 1991. Ground-water resources of Socorro County, New Mexico. US Geol. Surv. Water-Resour. Investig. Rep. 89-4083 108.
- S.S Papadopulous & Associates, 2000. Phase 2 Final Report for the Middle Rio Grande Water Supply Study. S.S Papadopulous & Associates, Inc.
- Szynkiewicz, A., Borrok, D.M., Ganjegunte, G.K., Skrzypek, G., Ma, L., Rearick, M.S., Perkins, G.B., 2015. Isotopic studies of the Upper and Middle Rio Grande. Part 2 — Salt loads and human impacts in south New Mexico and west Texas. *Chem. Geol.* 411, 336–350. <https://doi.org/10.1016/j.chemgeo.2015.05.023>
- Williams, A.J., Crossey, L.J., Karlstrom, K.E., Newell, D., Person, M., Woolsey, E., 2013. Hydrogeochemistry of the Middle Rio Grande aquifer system — Fluid mixing and salinization of the Rio Grande due to fault inputs. *Chem. Geol.* 351, 281–298. <https://doi.org/10.1016/j.chemgeo.2013.05.029>
- Woessner, W.W., 2007. Building a Compact, Low-Cost, and Portable Peristaltic Sampling Pump. *Ground Water* 45, 795–797. <https://doi.org/10.1111/j.1745-6584.2007.00346.x>
- Xu, W., Su, X., Dai, Z., Yang, F., Zhu, P., Huang, Y., 2017. Multi-tracer investigation of river and groundwater interactions: a case study in Nalenggele River basin, northwest China. *Hydrogeol. J.* 25, 2015–2029. <https://doi.org/10.1007/s10040-017-1606-0>
- Zhi, W., Li, L., Dong, W., Brown, W., Kaye, J., Steefel, C., Williams, K.H., 2019. Distinct Source Water Chemistry Shapes Contrasting Concentration-Discharge Patterns. *Water Resour. Res.* 55, 4233–4251. <https://doi.org/10.1029/2018WR024257>

# Quantifying Surface Water and Groundwater Exchanges in the Southern Albuquerque Basin

by

Ethan Williams

Permission to make digital or hard copies of all or part of this work for personal or classroom use is granted without fee provided that copies are not made or distributed for profit or commercial advantage and that copies bear this notice and the full citation on the last page. To copy otherwise, to republish, to post on servers or to redistribute to lists, requires prior specific permission and may require a fee.



ProQuest Number: 30244366

INFORMATION TO ALL USERS

The quality and completeness of this reproduction is dependent on the quality and completeness of the copy made available to ProQuest.



Distributed by ProQuest LLC (2023).

Copyright of the Dissertation is held by the Author unless otherwise noted.

This work may be used in accordance with the terms of the Creative Commons license or other rights statement, as indicated in the copyright statement or in the metadata associated with this work. Unless otherwise specified in the copyright statement or the metadata, all rights are reserved by the copyright holder.

This work is protected against unauthorized copying under Title 17,  
United States Code and other applicable copyright laws.

Microform Edition where available © ProQuest LLC. No reproduction or digitization of the Microform Edition is authorized without permission of ProQuest LLC.

ProQuest LLC  
789 East Eisenhower Parkway  
P.O. Box 1346  
Ann Arbor, MI 48106 - 1346 USA